Stoddard, P. R., Lynch, E. M., Farrell, D. P., Dosey, A. M., DiMaio, F., Williams, T. A., Kollman, J. M., Murray, A. W., & Garner, E. (2020). Polymerization in the actin ATPase clan regulates hexokinase activity in yeast. *Science*, *367*(6481), 1039-1042. https://doi.org/10.1126/science.aay5359

Polymerization in the Actin ATPase clan regulates hexokinase activity in yeast

Patrick R Stoddard[1,2], Eric M. Lynch[3], Daniel P. Farrell[3,4], Annie M. Dosey[3], Frank DiMaio[3,4], Tom A. Williams[5], Justin M. Kollman[3], Andrew W. Murray[1,2*], Ethan C. Garner[1,2*]

[1] Department of Molecular and Cellular Biology, Harvard University, Cambridge, MA 02138, USA

[2] Center for Systems Biology, Harvard University, Cambridge, MA 02138, USA

[3] Department of Biochemistry, University of Washington, Seattle, WA 98195, USA

[4] Institute for Protein Design, University of Washington, Seattle, WA 98195, USA

[5] School of Biological Sciences, University of Bristol, Bristol BS8 1TQ, UK

[*] co-corresponding authors.

Correspondence should be addressed to awm@mcb.harvard.edu (AWM) and egarner@g.harvard.edu (ECG).

One-sentence summary

Yeast glucokinase activity is limited by its polymerization, which is critical for cell viability during glucose refeeding.

The actin fold is found in cytoskeletal polymers, chaperones, and various metabolic enzymes. Many actin-fold proteins, like the carbohydrate kinases, do not polymerize. We found that Glk1, a *Saccharomyces cerevisiae* glucokinase, forms two-stranded filaments with unique ultrastructure, distinct from other cytoskeletal polymers. In cells, Glk1 polymerized upon sugar addition and depolymerized upon sugar withdrawal. Polymerization inhibits enzymatic activity; the Glk1 monomer-polymer equilibrium sets a maximum rate of glucose phosphorylation regardless of Glk1 concentration. Mutation eliminating Glk1 polymerization alleviated concentration-dependent enzyme inhibition. Yeast containing non-polymerizing Glk1 were less fit when growing on sugars and more likely to die when refed glucose. Glk1 polymerization arose independently from other actin-related filaments and may allow yeast to rapidly modulate glucokinase activity as nutrient availability changes.

The Actin ATPase clan (*1*) is a diverse group of structurally similar protein families found in all domains of life (*2*). Several of the Actin ATPase families form polymers, but the metabolic enzymes, such as hexose kinases, do not (*3*). It is unclear if polymerization evolved several times within this clan or if these polymerizing families descend from a single, ancient, polymerizing ancestor, a hypothesis suggested by phylogenetic (*4*) and structural studies (*5*).

Cells use several mechanisms to change enzyme activity in response to environmental changes, including allosteric and post-translational regulation. Enzymes can also change their physical state, assembling into filaments or gels, which serves as a sensitive, tunable way to control activity. Enzyme polymerization can regulate flux through pathways (*6*), store enzymes during starvation (*7*), and measure and signal cellular states (*8*).

Hexokinases and glucokinases of fungi are from a single family (the hexokinase family) within the Actin ATPase clan. Fungal glucokinases phosphorylate glucose, mannose, and glucosamine, while the fungal hexokinases also phosphorylate fructose. The glucokinases have a higher substrate affinity and lower V_{max} than the hexokinases (*9*). *S. cerevisiae* has three hexokinase family proteins: a glucokinase (Glk1) and two hexokinases (Hxk1 and Hxk2). Hxk2 is expressed in glucose-rich environments and regulates the expression of the other two enzymes; Hxk1 and Glk1 repression is alleviated without glucose (*10*) (Fig. S1).

To probe the cell biology of these isozymes we made monomeric-superfolder-GFP (msfGFP) fusions to each at their native loci and examined their behavior in cells. Without glucose, Glk1-

msfGFP was diffuse. When glucose-starved cells were refed glucose, Glk1-msfGFP formed filamentous structures, which rapidly disassembled upon glucose removal (Fig. 1A-C; Movies S1-2). Glk1-msfGFP also polymerized upon refeeding other Glk1 substrates: mannose or glucosamine (Fig. S2; S3). Hxk1-msfGFP and Hxk2-msfGFP did not oligomerize (Fig. 1A).

To understand what regulates Glk1 polymerization, we studied it in vitro. Other enzymes form condensates in low pH (*7*), however Glk1 did not (Fig. S4). Rather, Glk1 polymerized in the presence of its substrates (ATP and glucose, mannose, or glucosamine) or its products (ADP and sugar-6-phosphate). Modest polymerization also occurred with Glk1 inhibitors (Fig. 1D; S5; S6) (*9*). Although fructose and galactose induced Glk1 polymerization in vivo, they did not in vitro, suggesting in vivo polymers assemble when cells convert these sugars into glucose-6-phosphate (G6P) (Fig. S2; S3; S7) (*11*, *12*).

Like actin, Glk1 exhibits a critical concentration (CC) for polymerization. Beneath 2 μM Glk1 there was no polymerization. Above 2 μM the concentration of Glk1 polymer increased, while unpolymerized Glk1 remained constant (Fig. 1E). This is consistent with the lack of polymers in fermenting cells where Glk1 expression is suppressed by glucose. Indeed, Glk1-msfGFP polymers were observed in glucose when Glk1-msfGFP was expressed from a strong promoter (Fig. S9). Consistent with the rapid polymerization observed in vivo, in vitro Glk1 polymerization reached steady state in a matter of seconds (Fig. 1G).

Polymerization can either activate or inhibit enzyme activity (*6*, *13*), so we measured Glk1 activity as we varied Glk1's concentration. Beneath Glk1's CC, G6P production rate increased

with Glk1. Above the CC the rate of product formation was constant (Fig. 1E). Thus, polymerization inhibits Glk1 activity, and the monomer-polymer equilibrium caps monomer concentration, thereby keeping net enzymatic activity constant.

We used electron microscopy of negative stained samples to examine Glk1 oligomers. Glk1 formed helical filaments in the presence of substrates (Fig. 1F). The micron-scale structures seen in vivo are likely driven by crowding (*14*), filament binding proteins (*15*, *16*), or dimerization of the fluorescent tag (*17*). Similar polymers were observed when Glk1 was fused to other "monomeric" fluorescent proteins (Fig. S8).

To investigate why Glk1 polymerizes and Hxk1 and Hxk2 do not, we solved the crystal structure of Glk1 (Table S1) (*18*). Comparing this to the *S. cerevisiae* Hxk2 structure (*19*) revealed differences in key regions: the N- and C-termini and in two loops (Fig. 2A; S10; S11). We then used cryo-electron microscopy to determine the structure of Glk1 filaments (Table S2) (*20*). This 3.8 Å resolution structure (Fig. 2B) revealed that Glk1 formed two-stranded, antiparallel filaments. Similar to other actin-like filaments (*4*), subunits were in the closed state and ligand bound (Fig. 2C; S13) (*21*), but unlike actin, did not flatten. Glk1 homologs alternate between open and closed states during their catalytic cycle (*21*), thus Glk1 inhibition likely arises from their inability to transition between states.

The interactions between Glk1 subunits along a strand differ from the conserved interactions in other Actin ATPase clan polymers (*5*) (Fig. S14). Along the strand, the N-terminal, solvent-exposed Phe3 of one subunit inserts into the hydrophobic pocket at the C-terminus of the next

(Fig. 2D-E; S15). Lateral associations between strands are mediated by the helix-loop-helix between residues 371-393, which binds antiparallel to the same region on the adjacent subunit (Fig. 2F).

Phylogenetically, the fungal glucokinases and hexokinases form separate clades. The group of yeast containing *S. cerevisiae* (the Saccharomyceteceae) arose ~200 million years ago. The Glk1 homologs in most Saccharomyceteceae contain four conserved motifs missing in both the other Glk1 homologs and all Hxk1/2 homologs. These motifs are at or near filament contacts: the N- and C-termini, loop 230-243, and loop 438-444. To test if these motifs predict polymerization, we purified different Glk1and Hxk1/2 homologs and tested their ability to polymerize. Only Glk1 homologs that contained all four motifs polymerized (Fig. S10; S16). Phylogenetic logistic regression showed these motifs correlate significantly with polymerization (P=0.018). These results suggest that Glk1 polymerization arose ~200 million years ago. One ascomycete lineage, the Kluveromycetes, lost this ability (Fig. 3A) (*22*, *23*).

The hexokinase family, which contains Glk1, segregates from the known polymer forming Actin ATPase families (Fig. 3B). This pattern is consistent with pairwise similarity between Hidden Markov Models of each family (Fig. S17; Table S3), and several lines of evidence suggest that Glk1 polymerization evolved independently of other actin-fold polymers: A) polymerizing Glk1 sequences form a subclade within the hexokinase family (Fig. 3A); B) that broader hexokinase family is monophyletic in the global actin-fold tree (Fig. 3B, 100% bootstrap, 100% SH-aLRT, 1 aBayes); C) hexokinases robustly group with the non-polymerizing glucokinases and ROK

kinases (96%, 95%, 1), and D) the monophyly of Glk1s with other polymerizing actins was rejected by an AU-test (P = 0.00106).

Next we examined how disrupting Glk1's polymerization affected enzymatic activity and cell physiology. To create non-polymerizing Glk1 (NonPol-Glk1), we mutated the N-terminal phenylalanine involved in inter-subunit contacts to serine (Glk1-F3S). This mutation eliminated polymerization both in vitro, and in vivo (Fig. S18A-B). NonPol-Glk1 was enzymatically active but lacked the concentration-dependent inhibition of wild-type Glk1 (Fig. S18C).

To distinguish between the cellular effects of a lack of inhibition and the absence of polymers, we mutated the catalytic lysine (K182A) (Fig. S13B) (*24*) to create catalytically dead Glk1 (CatDead-Glk1). We combined these mutations (F3S/K182A) to create non-polymerizing, catalytically dead Glk1 (NonPolCatDead-Glk1). CatDead-Glk1 formed polymers in vivo and in vitro but did not generate G6P. NonPolCatDead-Glk1 neither polymerized nor produced G6P (Fig. S18A-C).

When starved yeast are refed glucose, excess sugar kinase activity is toxic due to an imbalance between the early steps of glycolysis, which consume ATP, and the late steps, which generate ATP (*25*). Hxk1 and Hxk2 activity is inhibited by trehalose-6-phosphate, a transiently-accumulating metabolite (*26*). Because Glk1 is not inhibited by trehalose-6-phosphate, we hypothesized that Glk1 polymerization limits activity when starved cells are refed glucose. Consistent with this model, when cells grown in galactose were refed glucose, 15% of NonPol-Glk1 cells die (Fig. 4A). This death was caused by unregulated Glk1 activity and not lack of

Glk1 polymers: *glk1*Δ, CatDead-Glk1, or NonPolCatDead-Glk1 behaved indistinguishably from wild-type cells. Thus, Glk1 polymerization limits the rate of glucose phosphorylation during glucose refeeding.

Unregulated Glk1 activity is detrimental to fitness over the entire growth cycle. We used differential fluorescent labeling to compare the fitness of wild-type cells against each mutant. We grew mixed cultures to saturation, diluted them into fresh medium every 48 hours, and measured the proportion of strains by flow cytometry. NonPol-Glk1 cells had a substantial fitness defect in these conditions, averaging to a fitness cost of 6% (Fig. 4B) (*27*). In contrast, no growth defect was observed when mixed cultures were maintained in a glucose-rich environment (Fig. S19), suggesting that environmental changes are required to expose the growth defects of NonPol-Glk1 cells. Similar effects were observed competing these strains on other sugars (Fig. S20). Cells lacking Glk1 activity (*glk1*Δ, CatDead-Glk1, NonPolCatDead-Glk1) showed minor growth defects in acetate. Thus, Glk1 activity is important for growth on non-sugar sources and Glk1 polymerization prevents toxic overactivity during refeeding.

Glk1 polymerization governs its bulk rate of catalysis, with the Glk1 CC setting the upper limit of flux through the entire Glk1 pool (Fig. 4C). This mode of self-regulation is robust to growth state and cell-to-cell variation in protein level and it allows rapid adaptation to transient perturbations. In this sense, Glk1 polymerization behaves as a molecular surge protector, protecting the cell against nutrient spikes.

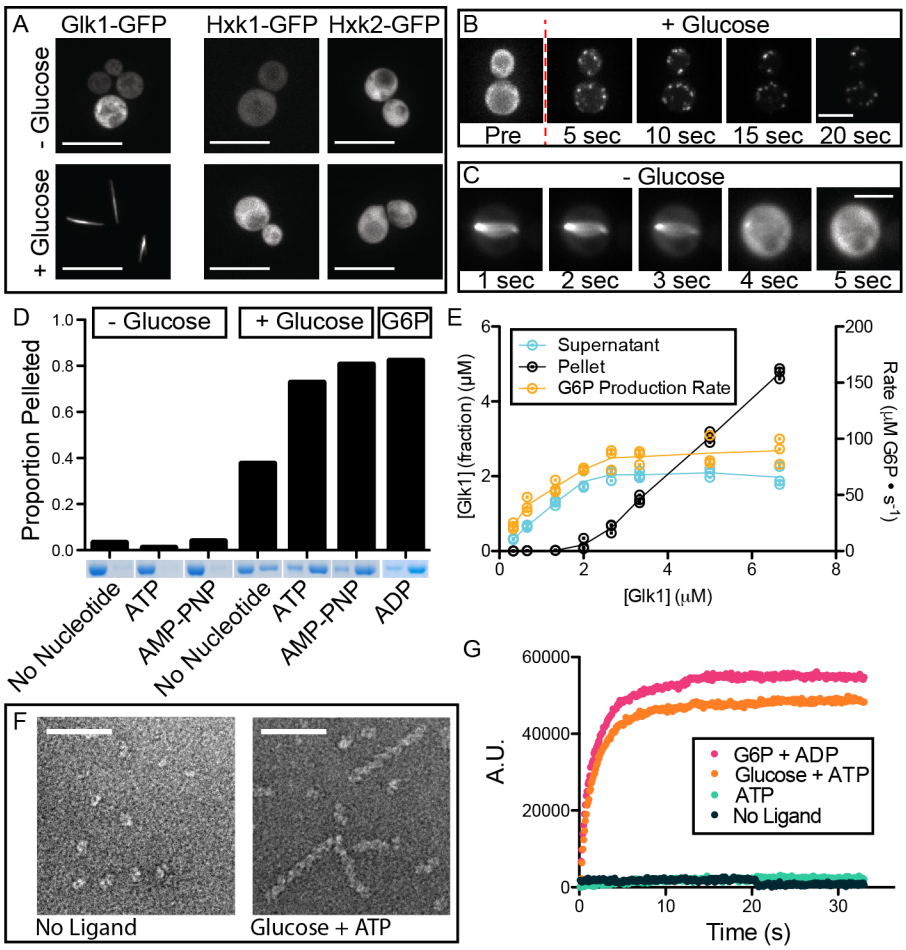

Fig 1. Glk1 forms filaments in response to its substrates at high enzyme concentration.

A) Fluorescence images of stationary phase Glk1-msfGFP (*left*), Hxk1-msfGFP (*middle*), and Hxk2-msfGFP (*right*) cells before (*top*) or after (*bottom*) glucose addition. Scale bars: 10 μm. **B, C)** Fluorescence images Glk1-msfGFP cells from a time-lapse video as glucose is added (*top)* or removed (*bottom*). Puncta in B eventually coalesce into a single, filamentous structure as in A and C. Scale bars: 5 μm. **D)** Purified Glk1 was ultracentrifuged at 436k x g for 30 min with different ligand combinations. The supernatant (*left*) and pellet (*right*) of each condition were subjected to SDS-PAGE. **E)** Purified Glk1 concentration was varied in saturating glucose and ATP and assayed for enzyme activity (glucose-6-phosphate production rate) or ultracentrifuged. The concentration of Glk1 in the supernatant and pellet was measured. N = 3. Means are

connected by lines. **F)** Electron micrographs of negative-stained samples: 7.5 µM Glk1 in the absence of ligands (*left*) or in saturating glucose and ATP (*right*). Scale bar: 50 nm. **G)** 90-degree light scattering of 7.5 µM Glk1 mixed with different ligand combinations.

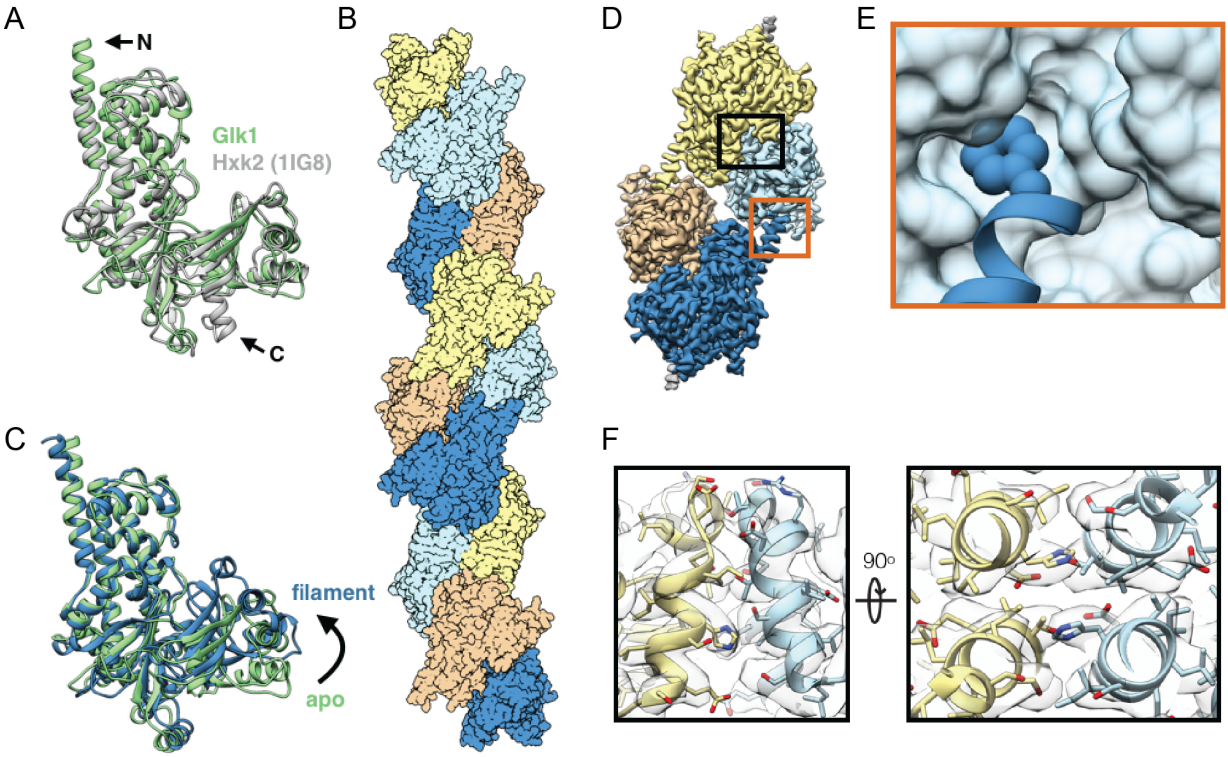

Fig 2. Glk1 forms anti-parallel, two-stranded filaments in its closed state

A: Superimposition of Glk1 crystal structure (*green*) (residues 1-500) with Hxk2 (PDB ID: 1IG8) (*19*) (*white*) (residues 18-486). The N-terminal helix of Glk1 extends further than that of Hxk2 (arrow, N), while the C-terminal helix of Hxk2 extends further (arrow, C). **B**: Surface representation of a model of Glk1 filaments reconstructed from cryo-EM (3.8 Å resolution). Glk1 filaments are two-stranded, anti-parallel helices. Subunits along each strand are either

orange/yellow or blue/cyan. **C**: Superimposition of the Glk1 crystal structure (*green*) with the Glk1 filament conformation from the cryo-EM reconstruction (*blue*). The crystal structure is not ligand bound and is in the open state while the filament form is ligand bound and in the closed state. **D**: Cryo-EM map of four subunits in the Glk1 filament colored by subunit. Longitudinal contact is boxed in orange, and a lateral contact is boxed in black. **E**: Closeup of longitudinal contact with Phe3 represented as van der Waals spheres and the next subunit represented as a surface model. Phe3 of one subunit inserts into the hydrophobic pocket near the next subunits C-terminus. **F**: Two orthogonal close-ups of lateral filament contact. The helix-loop-helix from residue 371-393 of one subunit (*yellow*) binds antiparallel to the same region of the adjacent subunit (*blue*). Cryo-EM map is transparent grey.

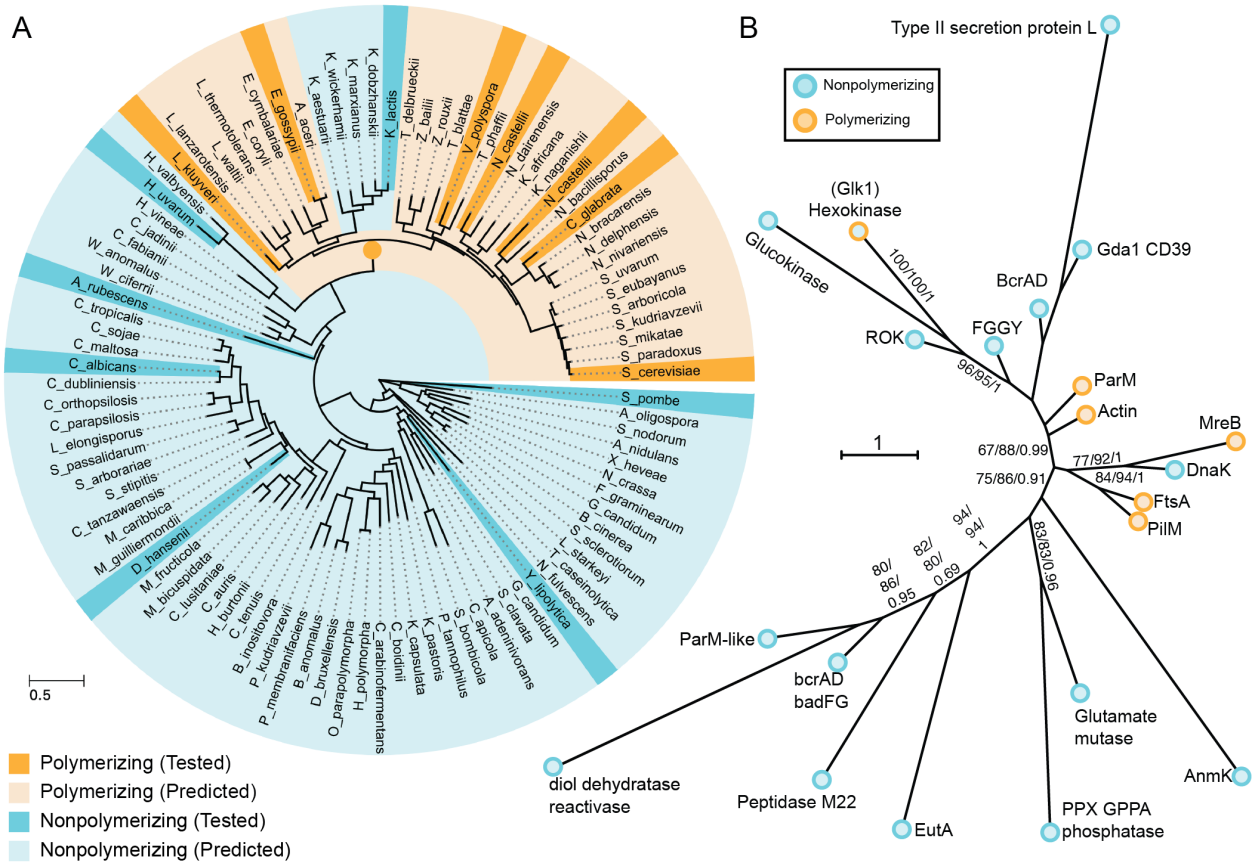

Fig 3. Glucokinase polymerization evolved independently of other actin-related polymers

A) Tree of ascomycetes as calculated by (*23*) indicating which species Glk1 homologs do (*dark orange*) and do not (*dark cyan*) polymerize. Species whose Glk1 homologs are predicted to polymerize based on conserved motifs (*pale orange*) and those predicted to not polymerize (*pale cyan*) are also indicated. Dark orange node marks the likely origin of Glk1 polymerization. **B)** Phylogeny of Actin ATPase families, summarizing phylogenetic analysis of 802 sequences from Actin ATPase protein families. A maximum likelihood tree was inferred under the LG+C20 substitution model in IQ-Tree (*28*). This displays the backbone structure of that ML tree with each family collapsed. Support values indicated are ultrafast bootstrap / SH-LRT / aBayes. Much of the backbone is uncertain; bootstrap supports shown when SH-LRT (middle value) > 70. This tree suggests the hexokinase family, which contains Glk1, forms a clade with ROK kinases and

glucokinases, and is only distantly related to other polymer forming actin families. Families that do not polymerize are cyan while families that do polymerize are orange. The full phylogeny is available online.

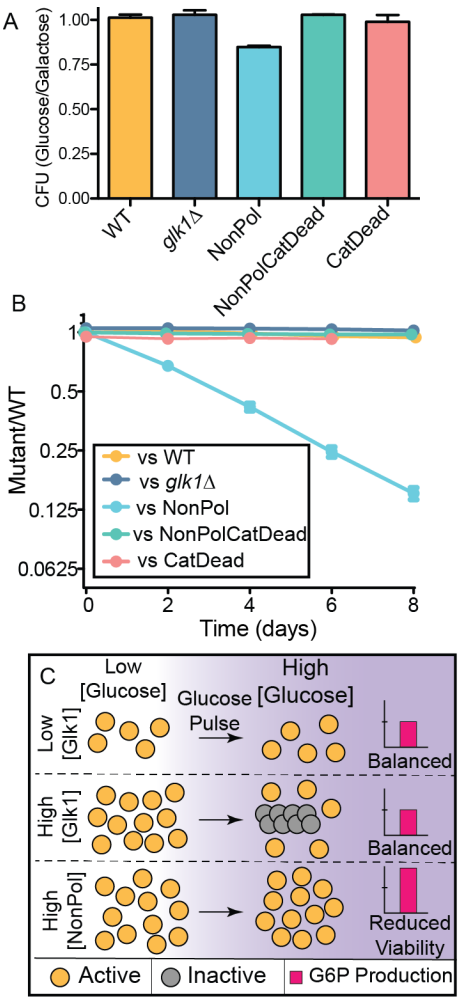

Fig 4. Elimination of Glk1 polymerization reduces fitness.

A) Cells were pre-conditioned in citrate buffered synthetic (CBS) medium with galactose and refed either glucose or galactose. The ratio of the resulting colonies are reported here. Mean +/- SD (N = 4). **B)** Wild-type cells expressing mCherry were competed against cells expressing GFP with different Glk1 genotypes through growth and dilution cycles in synthetic medium with glucose. The proportion of strains was measured after dilution by flow cytometry. Mean +/- SD (N = 5). **C)** Schematic of how Glk1 polymerization affects glucokinase activity. When Glk1 concentration is high and glucose increases, Glk1 polymerizes until the monomer concentration equals the CC. Glk1 polymers lack enzyme activity: regardless of Glk1 concentration, the

concentration of active enzyme is the same after glucose addition. When Glk1's ability to polymerize is disrupted, it's glucokinase activity is unconstrained, leading to fitness and viability defects.

References and Notes

1. S. El-Gebali *et al.*, The Pfam protein families database in 2019. *Nucleic Acids Res.* **47**, D427–D432 (2019).

2. B. Wickstead, K. Gull, The evolution of the cytoskeleton. *J. Cell Biol.* **194**, 513–525 (2011).

3. P. Bork, C. Sander, A. Valencia, An ATPase domain common to prokaryotic cell cycle proteins, sugar kinases, actin, and hsp70 heat shock proteins. *Proc. Natl. Acad. Sci. U.S.A.* **89**, 7290–7294 (1992).

4. P. R. Stoddard, T. A. Williams, E. Garner, B. Baum, Evolution of polymer formation within the actin superfamily. *Mol. Biol. Cell*. **28**, 2461–2469 (2017).

5. F. van den Ent, T. Izoré, T. A. Bharat, C. M. Johnson, J. Löwe, Bacterial actin MreB forms antiparallel double filaments. *Elife*. **3**, e02634 (2014).

6. R. M. Barry *et al.*, Large-scale filament formation inhibits the activity of CTP synthetase. *Elife*. **3**, e03638 (2014).

7. I. Petrovska *et al.*, Filament formation by metabolic enzymes is a specific adaptation to an advanced state of cellular starvation. *Elife*. **3**, 6063 (2014).

8. T. M. Franzmann *et al.*, Phase separation of a yeast prion protein promotes cellular fitness. *Science*. **359**, eaao5654 (2018).

9. P. K. Maitra, A glucokinase from Saccharomyces cerevisiae. *J. Biol. Chem.* **245**, 2423–2431 (1970).

10. A. Rodríguez, T. De La Cera, P. Herrero, F. Moreno, The hexokinase 2 protein regulates the expression of the GLK1, HXK1 and HXK2 genes of Saccharomyces cerevisiae. *Biochem. J.* **355**, 625–631 (2001).

11. P. A. Frey, The Leloir pathway: a mechanistic imperative for three enzymes to change the stereochemical configuration of a single carbon in galactose. *FASEB J.* **10**, 461–470 (1996).

12. J. B. Green, A. P. Wright, W. Y. Cheung, W. E. Lancashire, B. S. Hartley, The structure and regulation of phosphoglucose isomerase in Saccharomyces cerevisiae. *Mol. Gen. Genet.* **215**, 100–106 (1988).

13. E. M. Lynch *et al.*, Human CTP synthase filament structure reveals the active enzyme conformation. *Nat. Struct. Mol. Biol.* **24**, 507–514 (2017).

14. F. Hilitski *et al.*, Measuring cohesion between macromolecular filaments one pair at a time: depletion-induced microtubule bundling. *Phys. Rev. Lett.* **114**, 138102 (2015).

15. L. M. Griffith, T. D. Pollard, Cross-linking of actin filament networks by self-association and actin-binding macromolecules. *J. Biol. Chem.* **257**, 9135–9142 (1982).

16. H. Takatsuki, E. Bengtsson, A. Månsson, Persistence length of fascin-cross-linked actin filament bundles in solution and the in vitro motility assay. *Biochim. Biophys. Acta*. **1840**, 1933–1942 (2014).

17. D. Landgraf, B. Okumus, P. Chien, T. A. Baker, J. Paulsson, Segregation of molecules at cell division reveals native protein localization. *Nat. Methods*. **9**, 480–482 (2012).

18. P. R. Stoddard, E. C. Garner, A. W. Murray, PDBID: 6P4X, Crystal Structure of the S. cereviseae glucokinase, Glk1.

19. P. R. Kuser, S. Krauchenco, O. A. Antunes, I. Polikarpov, The high resolution crystal structure of yeast hexokinase PII with the correct primary sequence provides new insights into its mechanism of action. *J. Biol. Chem.* **275**, 20814–20821 (2000).

20. PDBID: 6PDT.

21. E. B. Kuettner *et al.*, Crystal structure of hexokinase KlHxk1 of Kluyveromyces lactis: a molecular basis for understanding the control of yeast hexokinase functions via covalent modification and oligomerization. *J. Biol. Chem.* **285**, 41019–41033 (2010).

22. A. Hagman, T. Säll, J. Piskur, Analysis of the yeast short-term Crabtree effect and its origin. *FEBS J.* **281**, 4805–4814 (2014).

23. X.-X. Shen *et al.*, Reconstructing the Backbone of the Saccharomycotina Yeast Phylogeny Using Genome-Scale Data. *G3 (Bethesda)*. **6**, 3927–3939 (2016).

24. J. Zhang *et al.*, Lys169 of human glucokinase is a determinant for glucose phosphorylation: implication for the atomic mechanism of glucokinase catalysis. *PLoS ONE*. **4**, e6304 (2009).

25. J. H. van Heerden *et al.*, Lost in transition: start-up of glycolysis yields subpopulations of nongrowing cells. *Science*. **343**, 1245114–1245114 (2014).

26. M. A. Blázquez, R. Lagunas, C. Gancedo, J. M. Gancedo, Trehalose-6-phosphate, a new regulator of yeast glycolysis that inhibits hexokinases. *FEBS Lett.* **329**, 51–54 (1993).

27. F. Duveau *et al.*, Fitness effects of altering gene expression noise in Saccharomyces cerevisiae. *Elife*. **7**, 173 (2018).

28. L.-T. Nguyen, H. A. Schmidt, A. von Haeseler, B. Q. Minh, IQ-TREE: a fast and effective stochastic algorithm for estimating maximum-likelihood phylogenies. *Mol. Biol. Evol.* **32**, 268–274 (2015).

29. N. A. Shevchuk *et al.*, Construction of long DNA molecules using long PCR-based fusion of several fragments simultaneously. *Nucleic Acids Res.* **32**, e19–19 (2004).

30. R. H. Schiestl, R. D. Gietz, High efficiency transformation of intact yeast cells using single stranded nucleic acids as a carrier. *Curr. Genet.* **16**, 339–346 (1989).

31. M. P. Malakhov *et al.*, SUMO fusions and SUMO-specific protease for efficient expression and purification of proteins. *J. Struct. Funct. Genomics*. **5**, 75–86 (2004).

32. D. G. Gibson, Enzymatic assembly of overlapping DNA fragments. *Meth. Enzymol.* **498**, 349–361 (2011).

33. C. A. Schneider, W. S. Rasband, K. W. Eliceiri, NIH Image to ImageJ: 25 years of image analysis. *Nat. Methods*. **9**, 671–675 (2012).

34. Z. Otwinowski, W. Minor, Processing of X-ray diffraction data collected in oscillation mode. *Meth. Enzymol.* **276**, 307–326 (1997).

35. A. J. McCoy *et al.*, Phaser crystallographic software. *J Appl Crystallogr*. **40**, 658–674 (2007).

36. P. Emsley, B. Lohkamp, W. G. Scott, K. Cowtan, Features and development of Coot. *Acta Crystallogr. D Biol. Crystallogr.* **66**, 486–501 (2010).

37. P. V. Afonine *et al.*, Towards automated crystallographic structure refinement with phenix.refine. *Acta Crystallogr. D Biol. Crystallogr.* **68**, 352–367 (2012).

38. C. Suloway *et al.*, Automated molecular microscopy: the new Leginon system. *J. Struct. Biol.* **151**, 41–60 (2005).

39. S. Q. Zheng *et al.*, MotionCor2: anisotropic correction of beam-induced motion for improved cryo-electron microscopy. *Nat. Methods*. **14**, 331–332 (2017).

40. K. Zhang, Gctf: Real-time CTF determination and correction. *J. Struct. Biol.* **193**, 1–12 (2016).

41. S. H. W. Scheres, RELION: implementation of a Bayesian approach to cryo-EM structure determination. *J. Struct. Biol.* **180**, 519–530 (2012).

42. A. Punjani, J. L. Rubinstein, D. J. Fleet, M. A. Brubaker, cryoSPARC: algorithms for rapid unsupervised cryo-EM structure determination. *Nat. Methods*. **14**, 290–296 (2017).

43. E. F. Pettersen *et al.*, UCSF Chimera--a visualization system for exploratory research and analysis. *J Comput Chem*. **25**, 1605–1612 (2004).

44. Y. Song *et al.*, High-resolution comparative modeling with RosettaCM. *Structure*. **21**, 1735–1742 (2013).

45. B. Frenz, A. C. Walls, E. H. Egelman, D. Veesler, F. DiMaio, RosettaES: a sampling strategy enabling automated interpretation of difficult cryo-EM maps. *Nat. Methods*. **14**, 797–800 (2017).

46. R. Y.-R. Wang *et al.*, Automated structure refinement of macromolecular assemblies from cryo-EM maps using Rosetta. *Elife*. **5**, 352 (2016).

47. P. Conway, M. D. Tyka, F. DiMaio, D. E. Konerding, D. Baker, Relaxation of backbone bond geometry improves protein energy landscape modeling. *Protein Sci.* **23**, 47–55 (2014).

48. G. M. Boratyn *et al.*, BLAST: a more efficient report with usability improvements. *Nucleic Acids Res.* **41**, W29–33 (2013).

49. S. Chojnacki, A. Cowley, J. Lee, A. Foix, R. Lopez, Programmatic access to bioinformatics tools from EMBL-EBI update: 2017. *Nucleic Acids Res.* **45**, W550–W553 (2017).

50. S. R. Eddy, Accelerated Profile HMM Searches. *PLoS Comput. Biol.* **7**, e1002195 (2011).

51. M. Steinegger *et al.*, HH-suite3 for fast remote homology detection and deep protein annotation. *bioRxiv*, 560029 (2019).

52. W. Li, A. Godzik, Cd-hit: a fast program for clustering and comparing large sets of protein or nucleotide sequences. *Bioinformatics*. **22**, 1658–1659 (2006).

53. K. Katoh, D. M. Standley, MAFFT multiple sequence alignment software version 7: improvements in performance and usability. *Mol. Biol. Evol.* **30**, 772–780 (2013).

54. S. Capella-Gutiérrez, J. M. Silla-Martínez, T. Gabaldón, trimAl: a tool for automated alignment trimming in large-scale phylogenetic analyses. *Bioinformatics*. **25**, 1972–1973 (2009).

55. D. T. Hoang, O. Chernomor, A. von Haeseler, B. Q. Minh, L. S. Vinh, UFBoot2: Improving the Ultrafast Bootstrap Approximation. *Mol. Biol. Evol.* **35**, 518–522 (2018).

56. A. Zhu, R. Romero, H. R. Petty, An enzymatic colorimetric assay for glucose-6-phosphate. *Anal. Biochem.* **419**, 266–270 (2011).

57. M. Johnston, J. S. Flick, T. Pexton, Multiple mechanisms provide rapid and stringent glucose repression of GAL gene expression in Saccharomyces cerevisiae. *Mol. Cell. Biol.* **14**, 3834–3841 (1994).

58. T. A. M. Bharat, G. N. Murshudov, C. Sachse, J. Löwe, Structures of actin-like ParM filaments show architecture of plasmid-segregating spindles. *Nature*. **523**, 106–110 (2015).

59. E. Behrmann *et al.*, Structure of the rigor actin-tropomyosin-myosin complex. *Cell*. **150**, 327–338 (2012).

60. J. Löwe, S. He, S. H. W. Scheres, C. G. Savva, X-ray and cryo-EM structures of monomeric and filamentous actin-like protein MamK reveal changes associated with polymerization. *Proc. Natl. Acad. Sci. U.S.A.* **113**, 13396–13401 (2016).

Acknowledgments: Special thanks to Quincey Justman for her gift of strains and extended discussions of this work. We thank Rachelle Gaudet for sharing beamtime and resources and for crystallographic advice, along with Christina Zimanyi, Lukas Bane, and Elizabeth May. We thank Jim Wilhelm for helpful discussions. We thank the Arnold and Mabel Beckman Cryo-EM Center at the University of Washington for access to electron microscopes. This work used NE-CAT beamlines (GM124165) at the APS (DE-AC02-06CH11357). Structures presented in this work are hosted online at the RCSB PDB (www.rcsb.org).

Funding: This work was supported by NIH grants DP2AI117923-01 to ECG, R01GM043987 to AWM, R01GM118396 to JMK, R01GM123089 to FD, F31GM116441 to PRS, and the NSF-Simons Center for Mathematical & Statistical Analysis of Biology at Harvard (#1764269) and the Harvard Quantitative Biology Initiative. ECG and PRS were also supported by Wellcome grant 203276/Z/16/Z, and support from the Volkswagen Foundation. TAW is supported by a Royal Society University Research Fellowship.

Authors Contributions: *S. cerevisiae* strains were cloned by PRS. Fluorescence microscopy was done by PRS. PRS measured the relative expression of Glk1 by flow cytometry. Plasmid construction and protein purification, in vitro measurements of polymerization and enzymatic

activity, Xray crystallography, Glk1 crystal structure refinement, and negative stain EM were done by PRS. PRS measured the viability of cells during glucose refeeding and measured the fitness of competed strains by flow cytometry. CryoEM sample preparation and data collection were performed by EML and AMD, cryoEM data was analyzed by EML and JMK, and the atomic model of Glk1 filaments was built by EML, DPF, and FD. Phylogenetic analysis of Actin ATPase families and regression analysis of polymerization-associated motifs was performed by TAW. This project was conceived of by PRS, ECG and AWM. PRS, EML, and TAW generated figures for this work and the paper was written by PRS, ECG, and AWM and edited by PRS, ECG, AWM, EML, JMK, and TAW.

Competing Interests

The authors have no competing interests.

Supplementary Materials:

Materials and Methods

Figures S1-S20

Tables S1-S4

Movies S1-S2

References 29 - 60

Supplementary Materials for

Polymerization in the Actin ATPase clan regulates hexokinase activity in yeast.

Patrick R Stoddard, Eric M. Lynch, Daniel P. Farrell, Annie M. Dosey, Frank DiMaio, Tom A. Williams, Justin M. Kollman, Andrew W. Murray*, Ethan C. Garner*

* co-corresponding authors.
Correspondence to: awm@mcb.harvard.edu (AWM) and egarner@g.harvard.edu (ECG).

This PDF file includes:

- Materials and Methods
- Figs. S1 to S19
- Tables S1 to S4
- Captions for Movies S1 and S2
- References 29 - 60

Other Supplementary Materials for this manuscript includes the following:

- Movies S1 and S2 available on the Science website
- The complete treefile used to create Figure 3B available on the Science website
- A high-resolution version of Table S3 available on the Science website

Materials and Methods

Strains and Culture Conditions

Unless otherwise noted, *S. cerevisiae* was grown at 30 ˚C in CSM supplemented with the appropriate carbon sources. For viability/plating assays, yeast were grown in citrate buffered synthetic medium (CBS) (*25*) with appropriate carbon source.

Plasmid Construction and Cloning

Table S4 lists strains and plasmids used in this study. Constructs for the transformation of *S. cerevisiae* were generated by fusion PCR (*29*), and the cells were transformed with purified PCR products (*30*). Clones were verified by amplification of the genomic locus followed by Sanger sequencing of the purified product.

Proteins were tagged with fluorescent proteins as C-terminal fusions using an 8 amino acid linker (GDGAGLIN).

For protein overexpression and purification from *E. coli,* glucokinases/hexokinases were cloned as his_6SUMO fusion constructs (*31*) into T7 plasmids by Gibson assembly (*32*). The plasmids were purified, and their sequences confirmed by Sanger sequencing using universal primers.

Media Transitions

Cells from cultures grown to saturation were loaded into a microfluidic cell (CellAsic), and their spent medium flowed over them. Cells were exchanged into fresh media containing 2 % glucose. Media was pumped at 2 PSI.

Microscopy

Images were taken on a Nikon Ti inverted microscope with a Yokogowa spinning disc confocal unit, 447, 488, 515, and 595 nm lasers, a Hamamatsu Orca camera operated with MetaMorph software. 8 µm z-stacks were taken in 0.2 µm increments. Z-stacks were converted to 8-bit, maximum intensity projection images, and contrast adjusted in ImageJ (*33*).

The filament disassembly video (Movie S2) was taken using Nikon Ti-E inverted microscope (Nikon) equipped with a 60× objective (PlanApo, numerical aperture 1.4, oil), GFP filter (Chroma Technology), and a CoolSNAP charge-coupled device camera (Photometrics) using streaming acquisition of a single focal plane.

Protein Purification

BL21(DE3) Rosetta containing the his_6SUMO fusion plasmid were grown to OD_{600} ~ 0.6 and induced overnight with 0.4 mM IPTG at 16 ˚C. His_6SUMO fusion products were purified and cleaved as in (*31*). Proteins were further purified and exchanged into HKM-buffer (20 mM HEPES-KOH pH 7.5, 100 mM KCl, 1 mM $MgCl_2$, 10 % glycerol (v/v), 10 mM β-mercaptoethanol) using an S200 16/600 column on an AKTA FPLC. Fractions were pooled and concentrated. Aliquots were snap frozen in liquid nitrogen and stored at -80˚C until needed.

Ultracentrifugation

Unless otherwise noted, polymerization reactions were done in HKM-buffer and contained 5 µM enzyme, 10 mM glucose, and 10 mM MgATP. Polymerization reactions were spun in a TLA-

100 (Beckman) at 100k rpm for 30 minutes at 30 ˚C. Supernatants were removed and added to equal volume of 2xSDS-Buffer. Pellets were resuspended by heating at 65 ˚C in 2 volumes of 1xSDS-Buffer. Fractions were subjected to SDS-PAGE, stained with Coomassie Blue G250, and band intensities were quantified in imageJ (*33*).

Light Scattering

Polymerization reactions were initiated by mixing 15 µM Glk1 with an equal volume of 10 mM glucose and 10 mM MgATP or 10 mM glucose-6-phosphate and 10 mM MgADP using a SFA-20 rapid mixer (Hi-Tech Scientific), driven by a pneumatic drive unit (Hi-Tech Scientific). The 90-degree scattering of the solution at 315nm was measured using a Fluorolog-3 (Horiba).

Crystallization, Diffraction, and Refinement

Glk1 was exchanged into 5 mM HEPES-KOH pH 7.5, 20 mM KCl, 1 mM $MgCl_2$, 0.5 mM TCEP and concentrated to 11 mg/mL by centrifugal ultrafiltration (Amicon Ultra; Millipore). Conditions were screened around the conditions used in (*9*) as hanging drops. Final crystallization conditions were 2.4 M $(NH_4)_2HPO_4$, 0.1 M CHES pH 9.4 (2:1 protein:well-solution) with crystals forming after 5 days at 20 ˚C. Crystals were cryoprotected by briefly soaking in well solution supplemented with 18 % glycerol before freezing.

X-ray data were collected at the Advance Photon Source beamline 24-ID-C at the Argonne National Laboratory. 180˚ of data was collected with a 10 µm beam at 20 % transmission. Reflection data were indexed, integrated, and scaled with HKL2000 (*34*). Initial phases were

obtained using Phaser (*35*) for molecular replacement, using the *S. cerevisiae* hexokinase-2 structure (PBD ID: 1IG8) (*19*) as a search model. The model was built in Coot (*36*) and refined using Phenix.refine (*37*). Positional and B-factor refinement with TLS, torsion angle, and NCS restraints were used. Phosphates from the crystallization condition were modeled into densities of appropriate size that were coordinated by basic and polar residues. The asymmetric unit of the crystal contained six protein chains. Residues 51-59 were omitted from all chains because this loop had poor density. Besides this omission, chains A, C, and F contain residues 1-500, chains B and E contain residues 3-500, chain D contains residues 4-500. Chain A was used for analysis and generation of figures.

CryoEM sample preparation and data collection

Glk1 was buffer-exchanged into 20 mM K-HEPES pH 7.5, 100 mM KCl, 1mM $MgCl_2$, and 0.5 mM DTT using a ZebaSpin 7K MWCO desalting column. Glk1 filaments were then formed by incubating 20 µM Glk1 with 10 mM glucose, 10 mM $MgCl_2$, and 10 mM ATP for 20 minutes at room temperature. CFLAT2/2 holey-carbon grids (Protochips Inc.) were glow-discharged using a PELCO easiGlow on the negative setting, with a current of 20 mA for 20 seconds at 0.39 mBar in air. To prepare samples for cryoEM, 2.5 µl Glk1 filament sample (20 µM) was applied to glow-discharged grids and blotted away 4 times successively, before being plunged into liquid ethane using a Vitrobot (FEI co.). The first 3 blots were performed manually by immediately touching Whatman Grade 1 filter paper to the edge of the grid to rapidly wick away solution (outside of the Vitrobot), with the final blot performed on the Vitrobot with standard filter paper (Ø55/20mm, Grade 595). The Vitrobot was set to room temperature and 100% humidity, with

blot force, wait time, drain time, and offset all set to 0. Data was collected on a Titan Krios (FEI co.) with a Quantum GIF energy filter (Gatan Inc.) operating in zero-loss mode with a 20 eV slit width. Movies were acquired on a K-2 Summit Direct Detect camera, operating in super-resolution mode with a pixel size of 0.525 Å/pixel, with 50 frames and a total dose of 90 electrons/$Å^2$. Leginon software was used for automated data collection (*38*).

CryoEM data processing

Movie frames were aligned, dose-weighted, and binned 2X using MotionCor2 (*39*), and CTF parameters were estimated using GCTF (*40*). Subsequent cryoEM processing steps are summarized in Figure S12. Helices were picked manually from a subset of images using Relion (*41*), exported to cryoSPARC (*42*), and used to generate initial 2D classes which were then used as templates for picking from all micrographs in cryoSPARC. Further 2D classification (4 rounds) was performed in cryoSPARC, and particles from good classes showing high-resolution features were exported to Relion. Relion 3D refinement produced a structure at 5.8Å resolution, and further masked refinement produced a structure at 3.9Å. The mask encompassed 4 subunits, and was used in all subsequent steps. Relion 3D classification was then performed, and particles contributing to the class with the highest resolution were selected for further refinement. In order to formally impose helical symmetry, initial estimates of helical symmetry were obtained by rigid body fitting of the Glk1 crystal structure into the 3.9Å cryoEM map, then measuring the translation and rotation between adjacent subunits in Chimera (*43*). These estimates (rise 59.9Å, rotation 119.7 degrees) were used as starting values for Relion 3D refinement with helical symmetry search, and the resulting refined helical symmetry values (rise 60.1Å, rotation 120.4

degrees) were then imposed in a final Relion 3D refinement. The final map was sharpened using Relion post-processing, and resolution was estimated at 3.8Å using the $FSC_{0.143}$ cutoff. Details of 3D reconstructions are summarized in Table S2.

Atomic model refinement

The Glk1 filament model was based on the solved crystal structure, PDB ID: 6P4X. First, small gaps in the model were resolved with RosettaCM (*44*) which used the model as a template and the cryoEM map EMD-20309 as a guide. Due to low convergence, residues 47-64 were removed, and completed with RosettaES (*45*). Next, the model was further refined using the density and fragment sampling as described in (*46*). Finally, all-atom refinement was performed in Cartesian space utilizing the Rosetta FastRelax (*47*) protocol. Model to map validation data was generated using phenix (*37*), and the Rosetta density_tools application (*46*).

Homolog Selection

Glucokinase and hexokinase homologs for purification and polymerization testing were found by reciprocal BLAST (*48*) searches and were informed by synteny when possible. Protein alignments of the tested enzymes were made using Clustal Omega (*49*).

Actin superfamily fold similarities

Our analyses were based on a dataset of HMMs representing each member of the actin fold family obtained from the Pfam database (version 32.0). For families in which the N and C terminal domain halves were represented by different Pfam HMMs (hexokinase, glucokinase,

and hydantoinase), we built new HMMs by searching the full-length query sequence of *S. cerevisiae* Glk1 (UniProtKB – P17709) for the hexokinases, the *E. coli* Glk (UniProtKB – P0A6V8) for the glucokinases, and the *E. coli* HyuA (UniProtKB – Q46806) for the hydantoinases against the UniProtKB database using Jackhmmer (*50*). Pairwise similarity comparisons between the HMMs were performed using HHsearch from the HH-Suite 3 package (*51*).

Actin fold phylogeny

The phylogeny was based on a set of sequences assembled previously (*4*), but updated to include the full set of folds analyzed here. Representative sequences for each fold were selected by CD-HIT (*52*) clustering of the highly redundant set of sequences used to construct the corresponding HMMs. Sequences were aligned using the L-INS-i mode in mafft (*53*), poorly aligning regions of the alignment were identified and removed using the "gappyout" mode in trimAl (*54*), and the phylogeny was inferred under the LG+C20+F model in IQ-Tree 1.6.10 (*28*). Bootstrap supports were computed using the UFBoot2 algorithm (*55*).

Glucokinase Activity Assays

Glucose-6-phosphate production was measured in HKM-buffer at 30 ˚C. Timepoints were quenched in an equal volume of 100 mM EDTA at 95 ˚C. Glucose-6-phosphate concentration was measured in each timepoint by a colorimetric enzyme-coupled reaction as in (*56*).

Competition Experiments

Strains were grown overnight in CSM with the appropriate carbon source, diluted into fresh medium and grown to mid exponential phase. mCherry labeled wild-type cells were mixed with GFP labeled strains in equal numbers. Cells were back diluted 200-fold every 48 hours, and samples taken two hours later. The ratio of the two strains was measured by flow cytometry (Fortessa) and the data analyzed in FlowJo (Beckton and Dickinson).

Viability Experiments

Strains were conditioned in CBS/Galactose for 48 hours, being diluted to $1x10^5$ cells/mL in fresh medium every 12 hours. Cells were harvested, washed twice in CBS with no carbon source, and plated onto either CBS/glucose or CBS/galactose. Colonies were counted after three days at 30 ˚C.

Supplemental Figures

Figure S1 – Glk1 expression under different growth conditions.

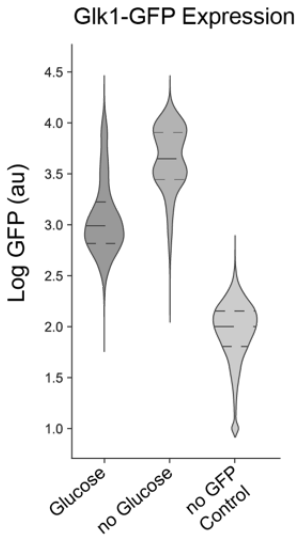

Green fluorescence of cells expressing Glk1-msfGFP from the Glk1 locus were measured by flow cytometry while growing in glucose or 12 hours after glucose was depleted from the culture (*no Glucose*). Middle line in each violin represents the median of the distribution. Upper and lower lines represent top and bottom quartiles. Glk1 expression increases in the absence of glucose. The no GFP Control shows the green autofluorescence of S. cerevisiae.

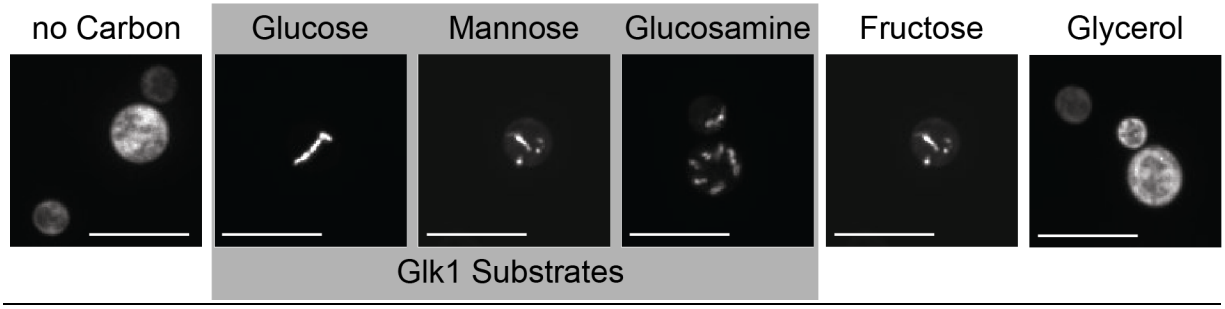

Figure S2 - Glk1-msfGFP polymerizes in cells in response to several sugars.

Maximum intensity projections of confocal z-stacks of Glk1-msfGFP cells. Cells were grown to saturation and washed in media containing no carbon. Cells were refed the sugar indicated, and fluorescence micrographs were taken 1 minute after refeeding. Carbon sources that are Glk1 substrates are boxed in gray. Scale bar: 10 µm.

Figure S3 – Galactose triggers Glk1-msfGFP polymerization only in galactose conditioned cells.

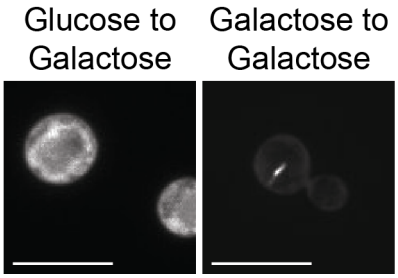

Fluorescence micrographs of cells expressing Glk1-msfGFP. Cells were either grown to saturation in glucose-containing medium or galactose containing medium. Glk1-msfGFP polymerizes in galactose conditioned cells when refed galactose but not in glucose conditioned cells. This is likely due to the suppression of the galactose transporter (Gal2) and galactokinase (Gal1) by the presence of glucose (*57*). Scale bar:10 µm.

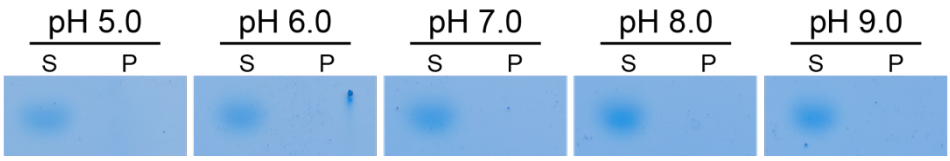

Figure S4 - Glk1 does not polymerize in response to change in pH.

10 µM Glk1 was ultracentrifuged at pH values from 5.0 to 9.0, and the supernatant (S, *left*) and pellet (P, *right*) were subjected to SDS-PAGE and stained with Coomassie blue.

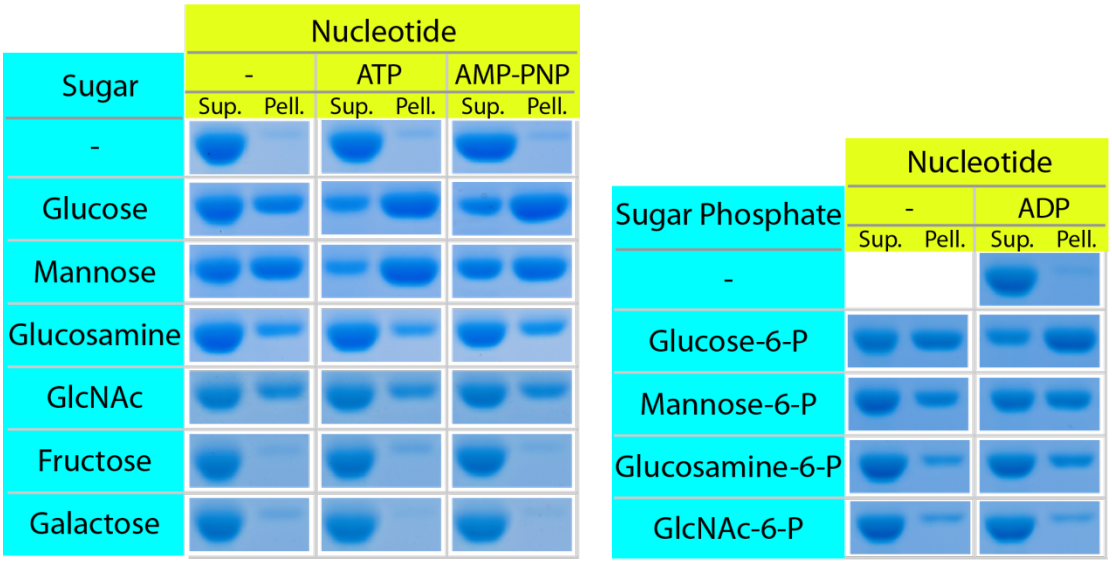

Figure S5 – Glk1 polymerization in the presence of different ligands.

Purified Glk1 was ultracentrifuged in the presence of different ligand combinations. The supernatant (*left*) and pellet (*right*) of each condition were subjected to SDS-PAGE. Glk1 polymerizes in response to its substrates (glucose, mannose, and glucosamine), inhibitors (GlcNAc and GlcNac-6-P), and products (glucose-6-P, mannose-6-P, and glucosamine-6-P), but not to other sugars (fructose and galactose).

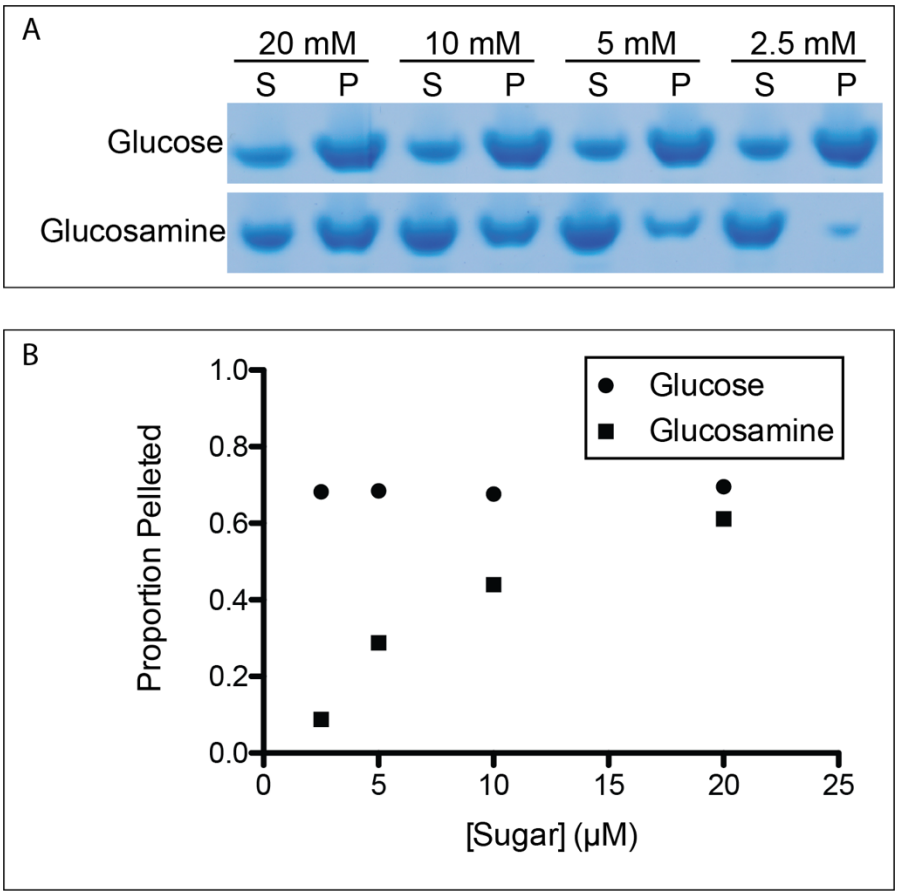

Figure S6: The difference in Glk1 pelleting efficiency with different ligands is from different ligand affinities. 6μM Glk1 with 10mM ATP and varied glucose and glucosamine concentration were spun at 436k x g for 30 min at 30 ˚C. The pellet and supernatant were subjected to SDS-PAGE and stained with Coomassie blue G250 (A). Quantification of the supernatant and pellet band at each concentration reveals that as glucosamine concentration increases, the amount of Glk1 in polymer approaches the amount in polymer in glucose (B).

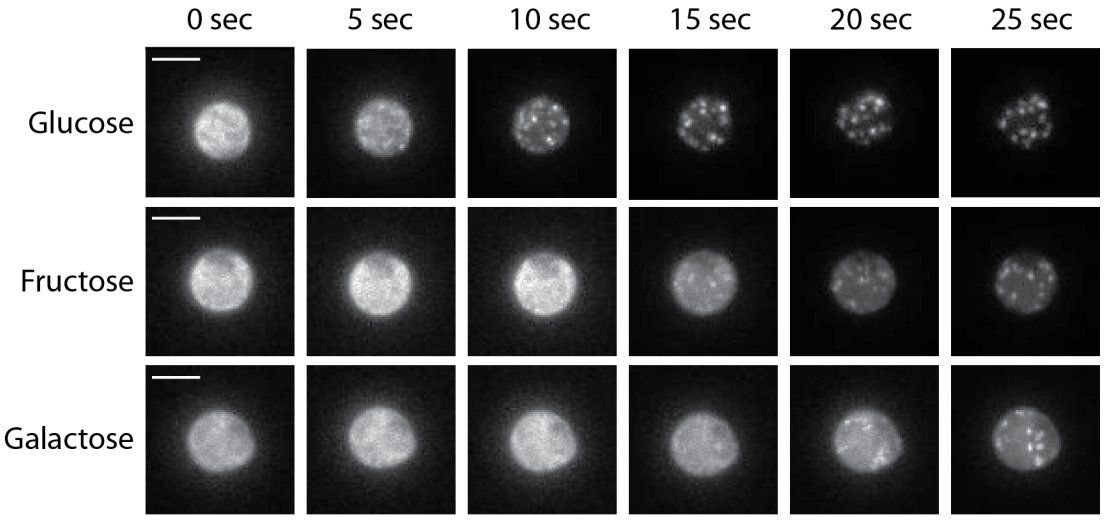

Figure S7 – Refeeding sugars that are not Glk1 substrates results in slower Glk1-msfGFP polymerization than refeeding glucose. Glk1-msfGFP cells grown to saturation on glucose (*top and middle*) or galactose (*bottom*) were refed glucose (*top*), fructose (*middle*), or galactose (*bottom*). Glucose caused polymerization more rapidly than either fructose or galactose. This is consistent with fructose and galactose causing polymerization in vivo by accumulation of glucose-6-phosphate. Scale bar: 5 µm.

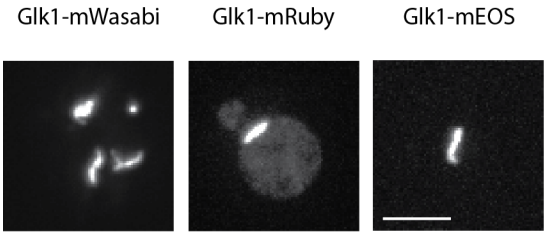

Figure S8 – Glk1 polymers look similar when other fluorescent tags are used.

Fluorescence micrographs of cells expressing Glk1-mWasabi (left), Glk1-mRuby (center), and Glk1-mEOS (right). Cells were grown to saturation and reintroduced to glucose before imaging. Scale bar: 5 µm.

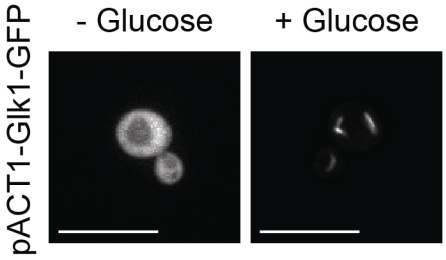

Figure S9 - Fluorescence micrographs of cells expressing Glk1-msfGFP under the Actin promoter.

Cells were harvested growing exponentially on glucose and imaged in the absence of glucose (*left*) or in the presence of glucose (*right*). Strong, constitutive expression of Glk1-msfGFP divorces cell state from polymer presence. Scale bar:10 µm.

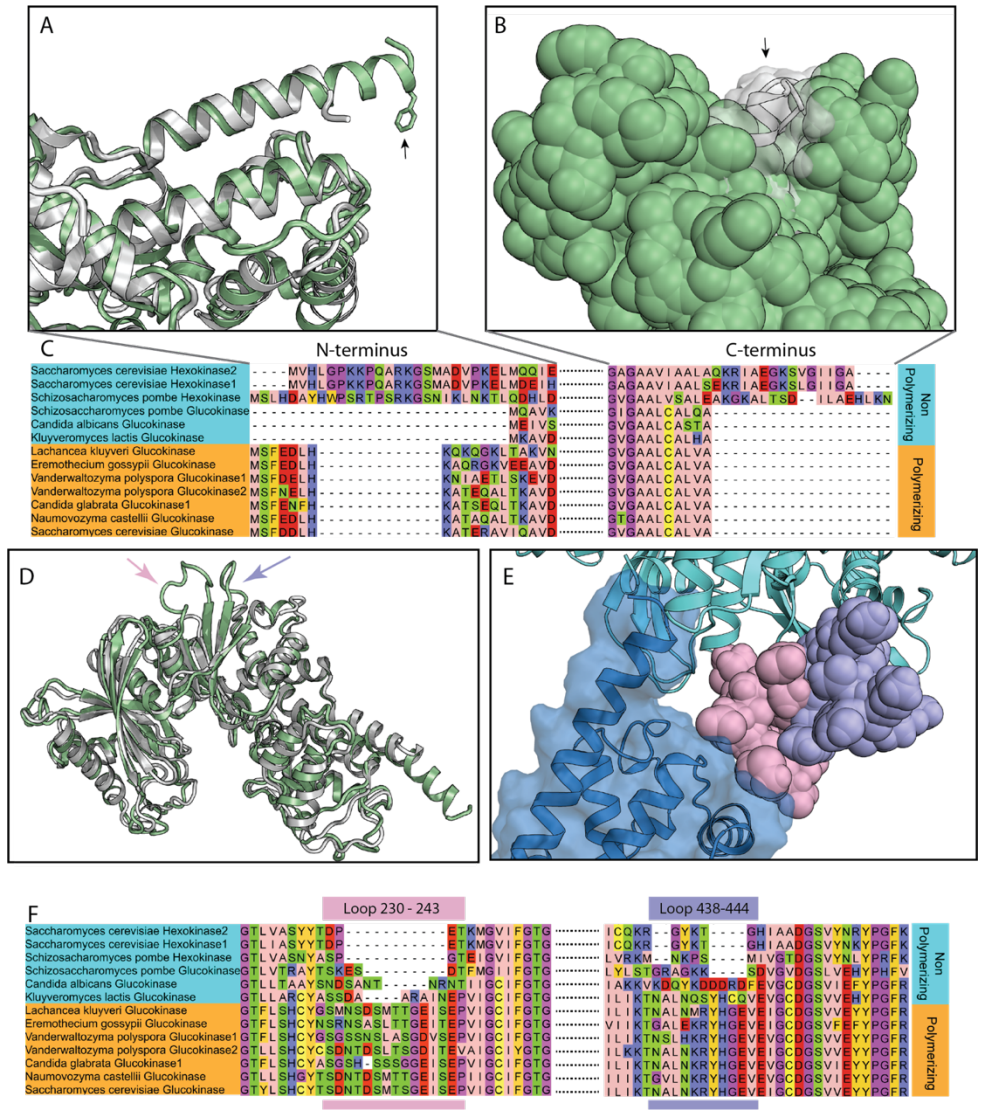

Figure S10 - Residues involved in Glk1 filament contacts are conserved amongst polymerizing glucokinases but not amongst non-polymerizing glucokinases or hexokinases.

A) Comparison of the N-terminus of Hxk2 (*white*, PDB ID: 1IG8) and Glk1 (*green*). The N-terminal helix of Glk1 extends beyond the body of the protein, while the N-terminal helix of Hxk2 ends flush to the body. Glk1's helix contains a solvent exposed phenylalanine. **B)** Models of Hxk2 and Glk1 show that the C-terminal helix of Hxk2 (*white ribbon/transparent surface*) extends beyond that of Glk1 (*green spheres*). This means that Hxk2 does not have the

hydrophobic pocket involved in Glk1 polymerization. **C)** Alignment of all tested enzymes. The N terminus (MSF(e/d)(e/d)LHK) and C-terminus (LCALVA) are conserved amongst enzymes that polymerize and divergent amongst enzymes that do not. **D)** The loop from Glk1 residue 230-243 (*pink arrow*), and Glk1 residue 438-444 (*purple arrow*) are larger than their corresponding loops in Hxk2 (*white*). **E)** Close up of longitudinal interface between two subunits in a model of a Glk1 filament. Loop 230-243 (*pink spheres*) contacts the next subunit (*blue ribbon and surface*), and loop 438-444 (*purple spheres*) packs tightly against loop 230-243. **F)** Alignment of all tested enzymes in loop regions. Both loops are extended in all polymerizing enzymes and are truncated or divergent in non-polymerizing enzymes.

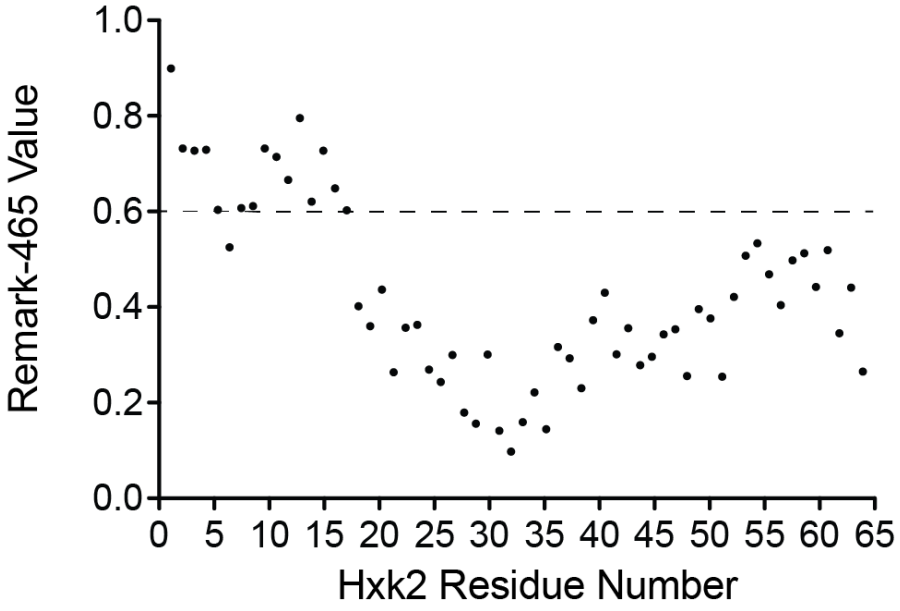

Figure S11 – The unmodeled residues in the Hxk2 crystal structure are likely disordered. The Remark-465 values of the first 65 residues of Hxk2. Values above 0.6 are more likely to be disordered. The first 16 residues are not modeled in the Hxk2 crystal structure (PDB ID: 1IG8), and this region is predicted to be disordered.

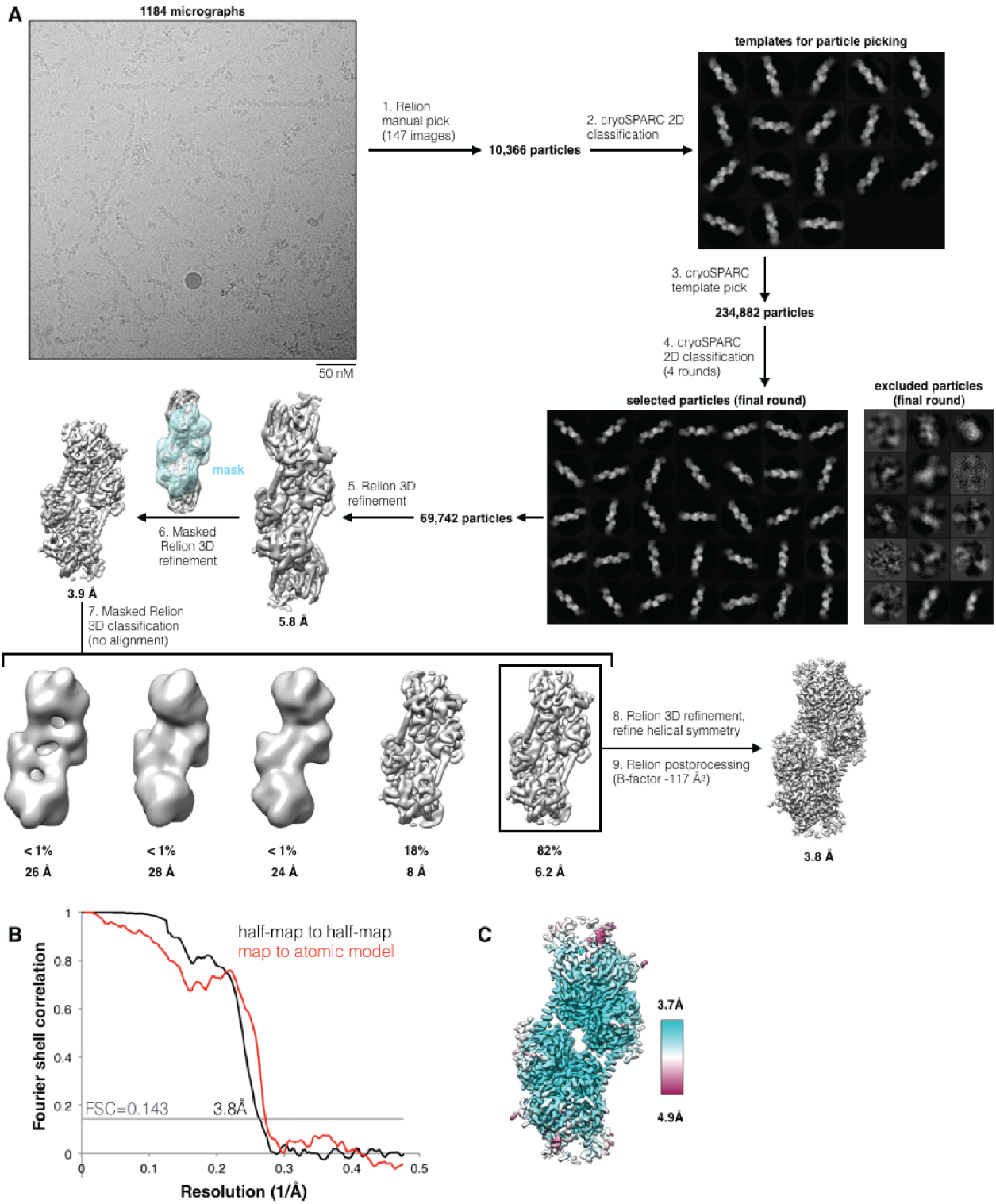
A
1184 micrographs
50 nM
1. Relion manual pick (147 images)
10,366 particles
2. cryoSPARC 2D classification
templates for particle picking
3. cryoSPARC template pick
234,882 particles
4. cryoSPARC 2D classification (4 rounds)
selected particles (final round)
excluded particles (final round)
5. Relion 3D refinement
69,742 particles
mask
6. Masked Relion 3D refinement
3.9 Å
5.8 Å
7. Masked Relion 3D classification (no alignment)
< 1%
26 Å
< 1%
28 Å
< 1%
24 Å
18%
8 Å
82%
6.2 Å
8. Relion 3D refinement, refine helical symmetry
9. Relion postprocessing (B-factor -117 Å²)
3.8 Å
B
half-map to half-map
map to atomic model
Fourier shell correlation
FSC=0.143
3.8Å
Resolution (1/Å)
C
3.7Å
4.9Å

Figure S12: CryoEM data processing and structure validation. (A) Flowchart of cryoEM data processing. Additional details are provided in the Methods section. (B) Half-map to half-map and map to atomic model FSC curves for the Glk1 filament structure. (C) Relion local resolution estimate of the Glk1 filament structure, showing a local resolution range of 3.7-4.9Å.

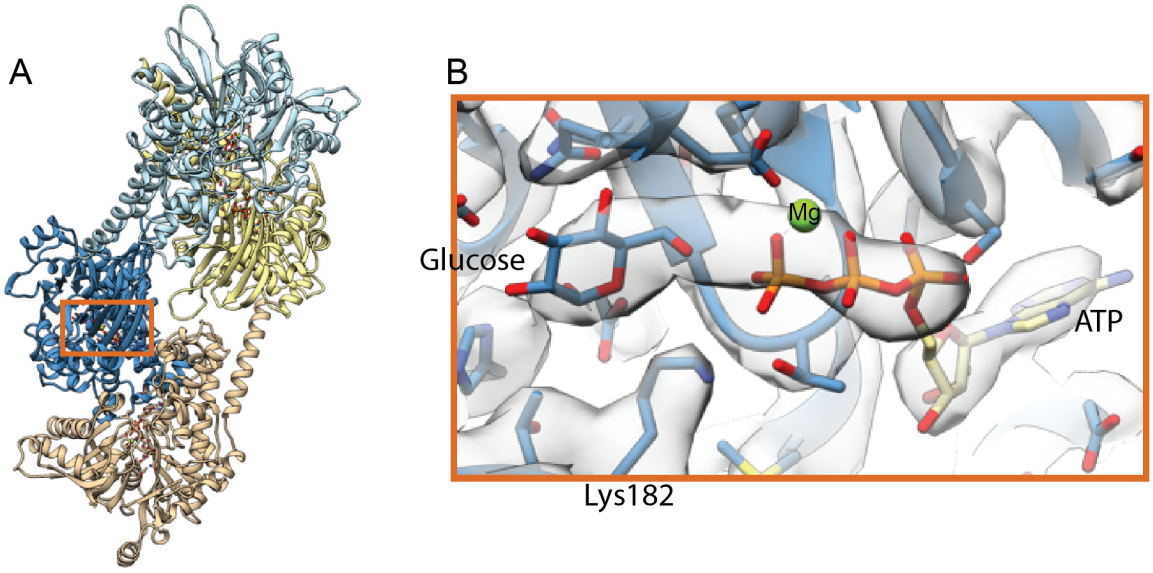

Figure S13 - Glk1 filaments have magnesium and glucose and ATP or G6P and ADP bound in their active site.

A) Cartoon representation of four subunits within a Glk1 filament showing where glucose and ATP are modeled within the filament. The orange box indicates the location of the ligands shown in B. **B)** Ligand density (*gray mesh*) is present in the cryoEM Glk1 filament electron density. Glucose and ATP vs G6P and ADP cannot be distinguished at this resolution. Here we have modeled glucose and ATP. The catalytic lysine (Lys182) can be seen coordinating the -OH on the 6-carbon of glucose and the -OH on the gamma-phosphate of ATP.

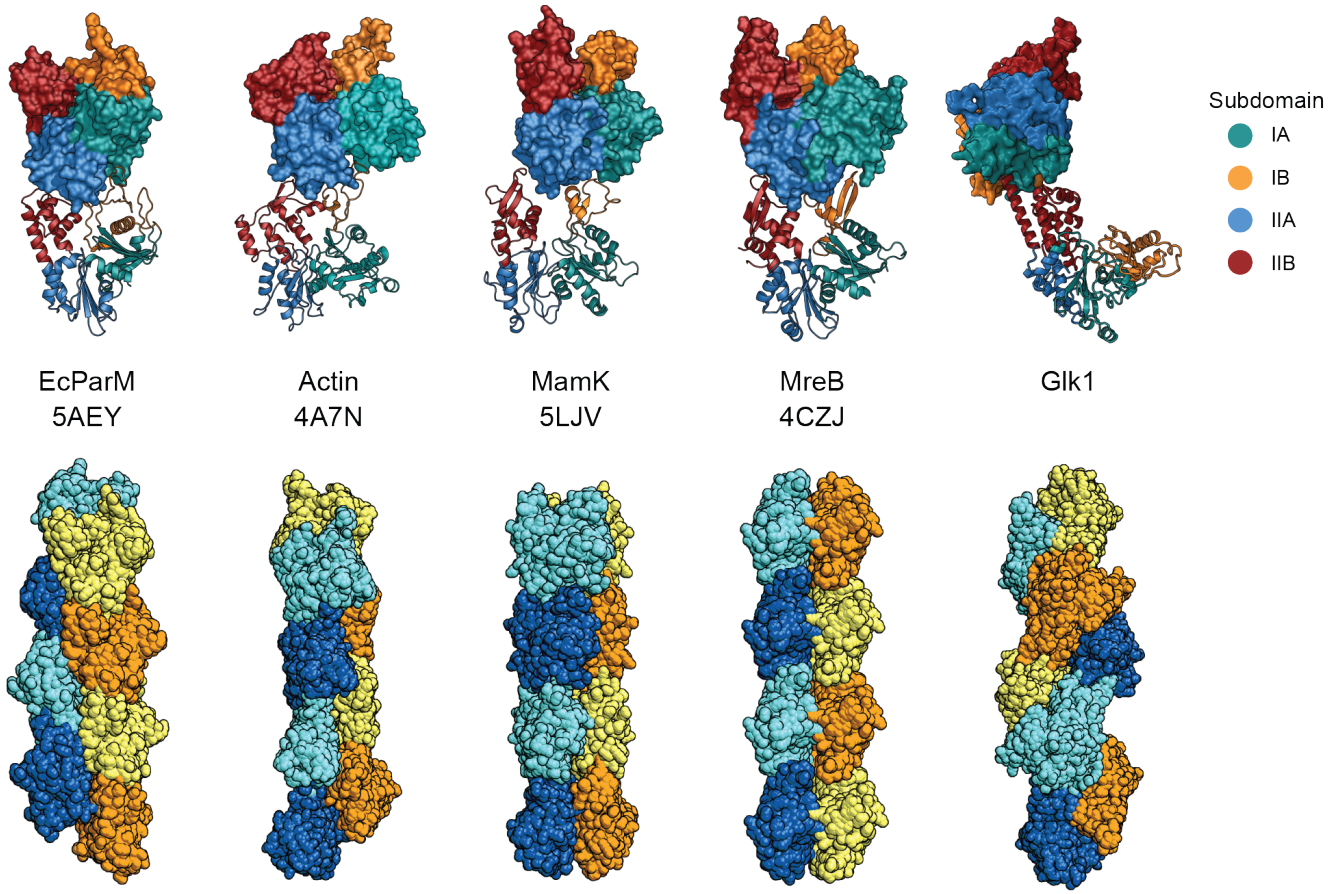

Figure S14 - Intersubunit geometry conserved in other actin-related filaments is not present in Glk1 filaments.

Top: Amongst all other actin-related filaments, along a single strand, subdomain IB and IIB contact subdomain IA and IIA respectively. In Glk1 filaments, subdomain IIB contacts subdomain IA (*5*, *58-60*). The top subunit is represented as a surface while the bottom subunit is represented as a ribbon.

Bottom: Despite the conserved geometry along strands in the cytoskeletal polymers, filaments are still able to achieve a variety of structures through varying subunit shape and lateral interactions.

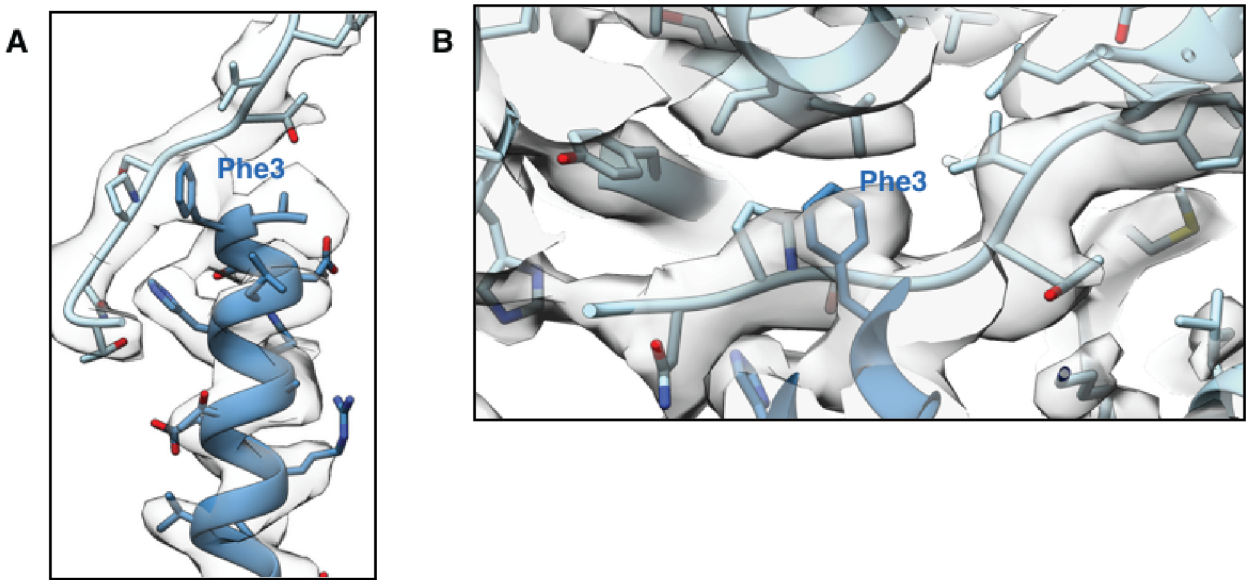

Figure S15 – CryoEM map at the longitudinal filament interface. (A) Isolated density for the N-terminal helix at the longitudinal filament interface. (B) cryoEM map around the Phe3 binding pocket.

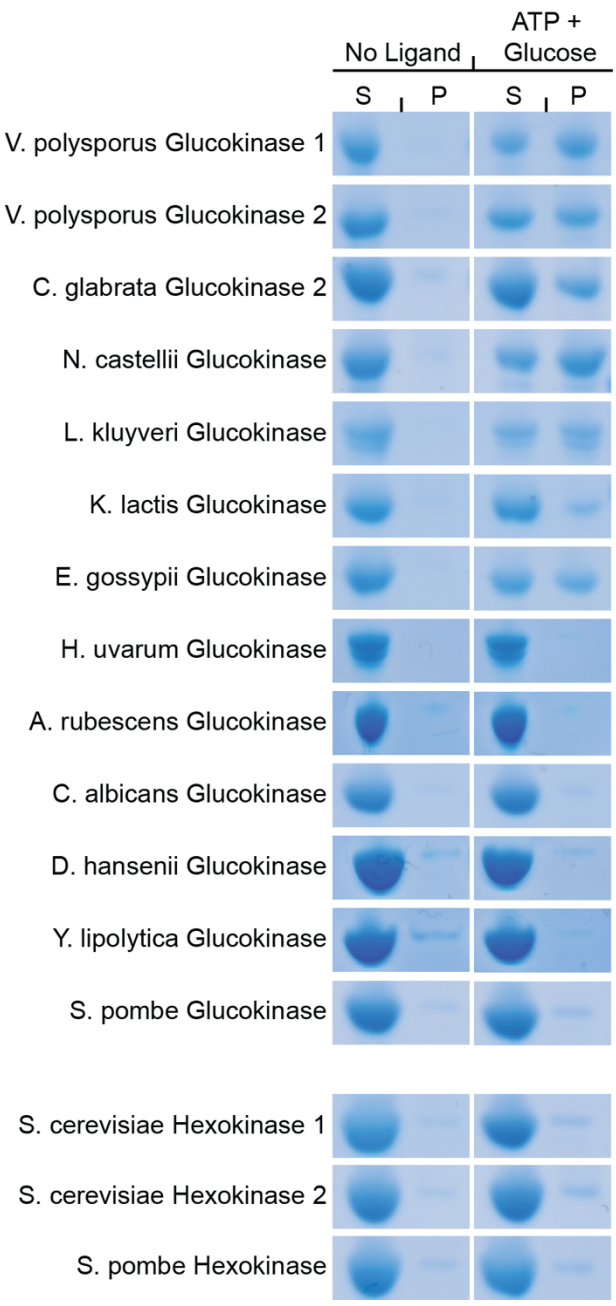

Figure S16 - Polymerization of Glk1 homologs.

Purified Glk1 homologs (glucokinases) and Hxk1/2 homologs (hexokinases) were ultracentrifuged in the absence of ligand (*left*) or the presence of glucose and ATP (*right*). The supernatant (*S, left*) and pellet (*P, right*) were subjected to SDS-PAGE and stained with Coomassie blue. Some other glucokinases polymerize in the presence of glucose and ATP while hexokinases do not.

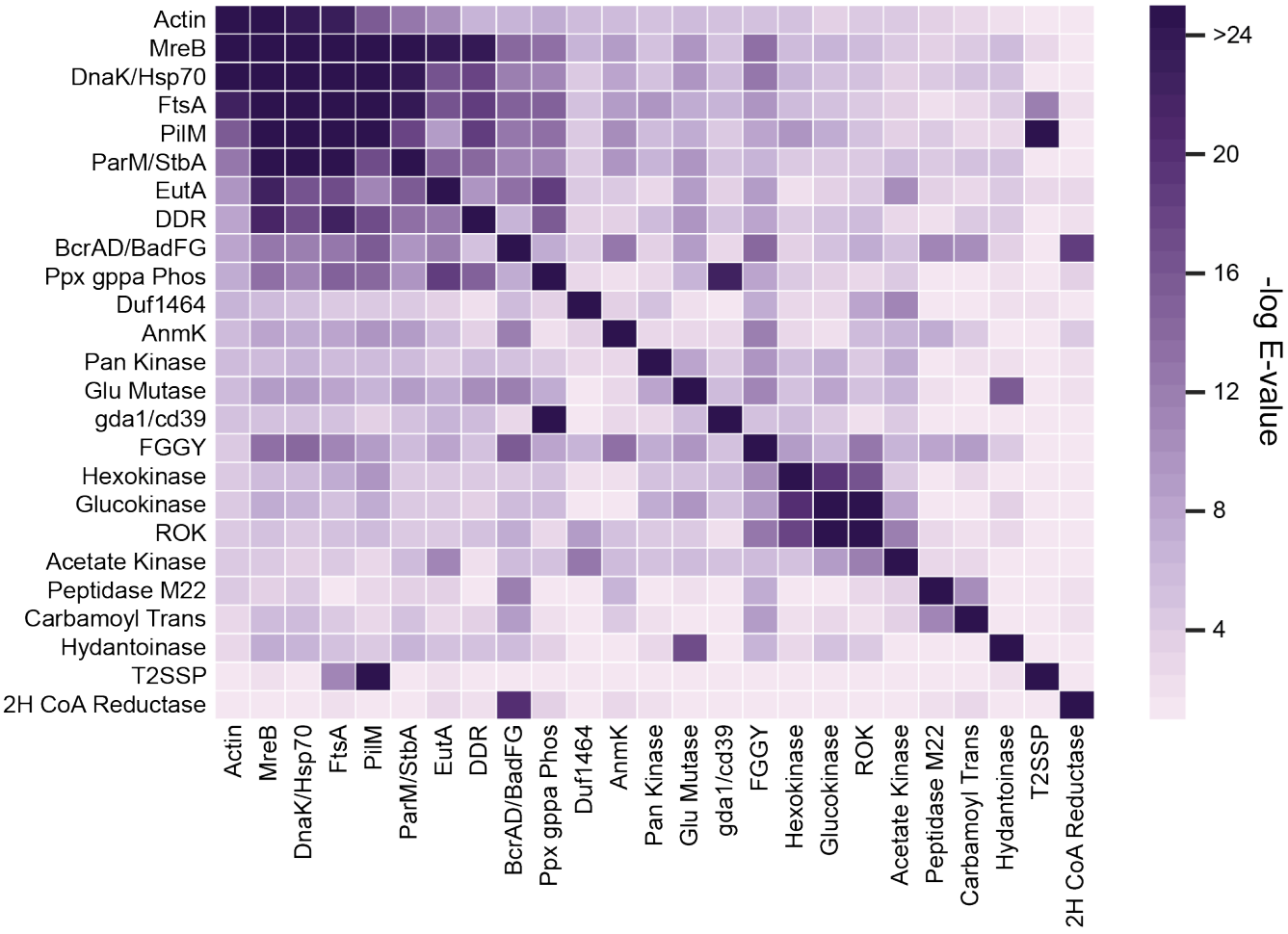

Figure S17 - Heatmap representing the e-value for the comparison of HMM for each protein family in the Actin ATPase clan.

The values are reported as negative logs of the e-value. Note that Glk1 is in the hexokinase, not the glucokinase family in this classification.

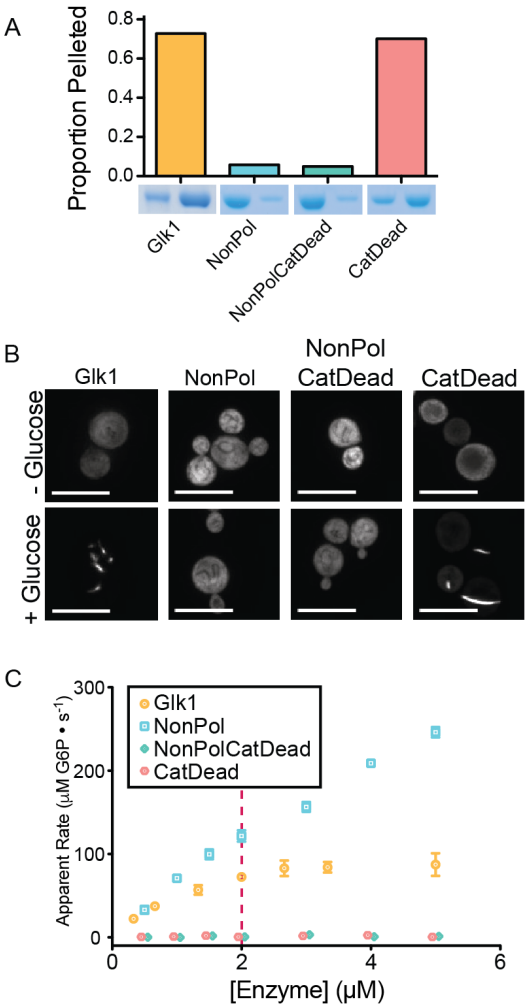

Figure S18 – Behavior of Glk1 Mutants: (A) 5 μM purified NonPol-Glk1, NonPolCatDead-Glk1, and CatDead-Glk1were ultracentrifuged with saturating glucose and ATP. The supernatant (*left*) and pellet (*right*) were subjected to SDS-PAGE and quantified. (B) Fluorescence images of: Glk1-msfGFP (*left*), NonPol-Glk1-msfGFP (*middle-left*), NonPolCatDead-Glk1-msfGFP (*middle-right*), or CatDead-Glk1-msfGFP (*right*) in stationary phase cells before (*top*) or after (*bottom*) refeeding glucose. Scale bar: 10 μm. (C) The rate of G6P production at different concentrations of purified Glk1, NonPol-Glk1, NonPolCatDead-Glk1, and CatDead-Glk1. Glk1's apparent rate does not increase beyond Glk1's CC (dashed line). Mean +/- SD (N = 3).

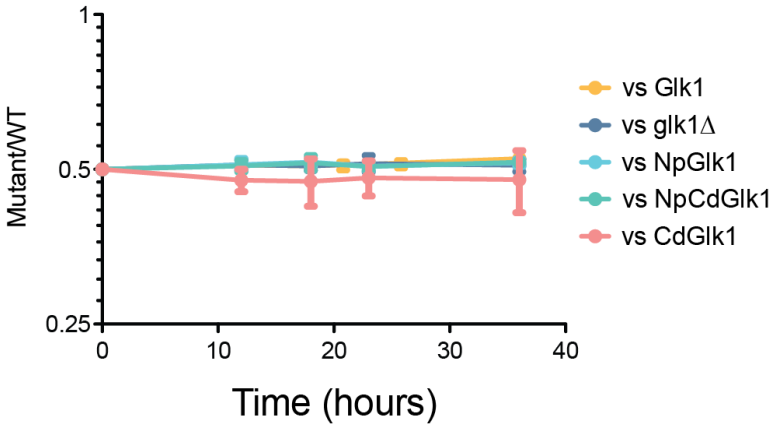

Figure S19 – Glk1 Mutants have no fitness effect during exponential growth on glucose. Wild-type W303 labeled with mCherry were grown in competition with green labeled W303 (wild-type, glk1Δ, NonPol-Glk1, NonPolCatDead-Glk1, CatDead-Glk1) in CSM-Glucose. Cultures were held at low cell density by repeated back dilution to ensure continuous fermentative, log-phase growth. In these conditions, none of the Glk1 mutants or the deletion of GLK1 yielded any significant growth effect. Mean +/- SD (N = 5).

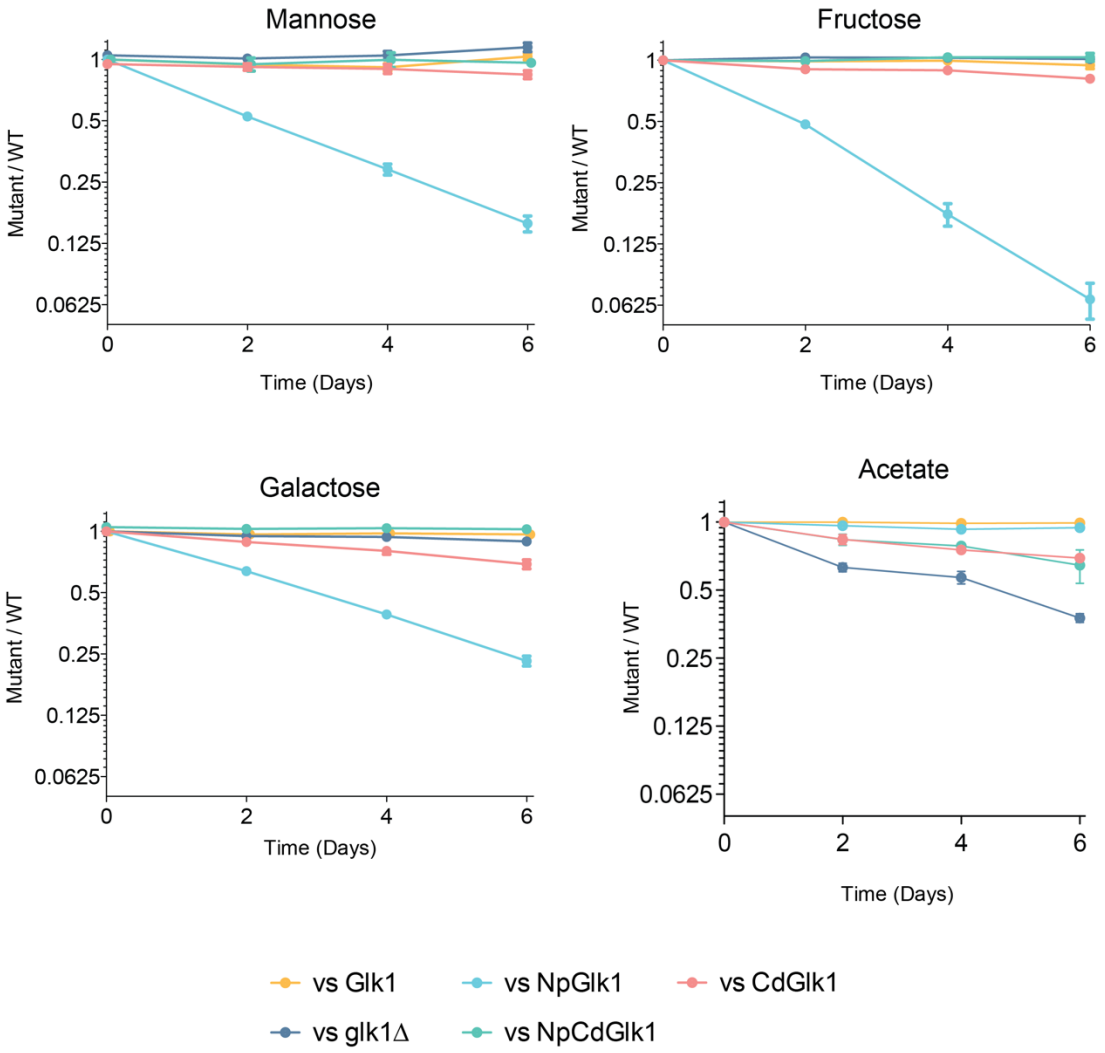

Figure S20 - NonPol-Glk1 cells have growth defects in a variety of sugars, but not on other carbon sources.

Wild-type W303 labeled with mCherry were grown to saturation and back-diluted every 48 hours in a mixed culture with green labeled W303 (wild-type, glk1Δ, NonPol-Glk1, NonPolCatDead-Glk1, CatDead-Glk1) in CSM-Mannose (*top-left*), CSM-Fructose (*top-right*), CSM-Galactose (*bottom-left*), or CSM-Acetate (*bottom right*). The relative proportion of the strains were measured after each dilution by flow cytometry. NonPolGlk1 cells showed reduced fitness when grown on all sugars tested. Cells lacking Glk1 activity (glk1Δ,

CatDeadGlk1, NonPolCatDeadGlk1) had reduced fitness when grown with acetate as the carbon source. Mean +/- SD (n=5).

Supplemental Tables

Table S1: Crystallography Statistics

	Glk1
Data Collection	
Wavelength (Å)	0.9793
Resolution Range (Å)	155.8 - 3.59 (3.718 - 3.59)
Space Group	P 43 21 2
Unit Cell (a,b,c)	174.5, 174.5, 323.9
Unit Cell (α,β,γ)	90, 90, 90
Number of Crystals	1
Total Reflections	122,662 (12,052)
Unique Reflections	61,332 (6,026)
Redundancy	2.0 (2.0)
Completeness (%)	99.97 (99.95)
Mean I/σ (I)	8.28 (1.56)
R-merge	0.100 (0.4831)
R-meas	0.142 (0.6832)
R-pim	0.100 (0.4831)
CC 1/2	0.988 (0.638)
Refinement	
Resolution Range (Å)	155.8 - 3.59 (3.718 - 3.59)
R-work	0.265 (0.336)
R-free	0.300 (0.357)
Number of Atoms	22,953
Reflections Used	61,332 (6,025)
Protein Atoms	22,888
Ligand Atoms	65
Protein Residues	2,944
Ramachandran Plot	
Favored (%)	98.73
Allowed (%)	1.27
Outliers (%)	0.0
RMS (bonds)	0.004
RMS (angles)	1.47
Wilson B-factor	91
Average B-factor	90
Protein B-factor	90
Ligands B-factor	76
Number of TLS Groups	20

Table S2: CryoEM Statistics

	Glk1 filament (EMD-20309, PDB 6PDT)
Data collection	
Electron microscope	Titan Krios
Voltage (kV)	300
Electron detector	K2 summit
Exposure time (s)	10
Total electron exposure ($e^-/Å^2$)	90
Magnification (nominal)	130,000X
Super-resolution pixel size (Å)	0.525
Frames collected/movie	50
Energy filter slit width (eV)	20
Automation software	Leginon
Micrographs collected	1184
Defocus range (μM)	-0.8 to -2.5
Reconstruction	
Pixel size (Å)	1.05
Particles extracted	234,882
3D Refinement package	Relion
Point group symmetry	D1
Refine helical symmetry	120.4°, 60.1Å
Particles in final reconstruction	56,778
Relion estimated accuracy rotations	1.945
Relion estimated accuracy translations	0.702
Unmasked resolution (0.5 FSC) (Å)	4.2
Unmasked resolution (0.143 FSC) (Å)	3.9
Masked resolution (0.5 FSC) (Å)	4.2
Masked resolution (0.143 FSC) (Å)	3.8
Local resolution range (Å)	3.7-4.9
B-factor for sharpening ($Å^2$)	-117
Model composition	
Protein residues	500
Ligands	ATP, glucose, Mg
Validation	
Clashscore	1.72
Poor rotamers	0
CC	0.66
RMSZ bond lengths	1.18
Bond lengths Z-score > 2 (%)	0.6
RMSZ bond angles	1.04
Bond angles Z-score > 2 (%)	0.2
Molprobity score	0.99
Clashscore	1.7
C-beta deviations	0
EMRinger score	1.7
CaBLAM outliers (%)	2.20
Ramachandran plot	
Favored (%)	98
Allowed (%)	2
Outliers (%)	0

Table S3: Table of negative log e-values for the pairwise comparison of the HMM for each protein family in the Actin ATPase clan. A high-resolution version of this table is in supplementary file S2.

	Actin	MreB	DnaKHsp70	FtsA	PilM	ParM/StbA	EutA	DDR	BcrAD/BadFG	ppx_gppa	DUF1464	AnmK	Pan_Kinase	Glu_Mutase	gda1/cd39	FGGY	Hexokinase	Glucokinase	ROK	Ace Kinase	Pep_M22	Carbam_Trans	Hydant	T2SSP	2H_CoA_red
Actin	171.333	34.443	23.917	22.026	15.53	12.455	10.637	6.908	6.502	7.543	5.809	5.915	5.006	5.599	4.768	5.185	4.962	3.912	4.605	4.51	3.507	2.847	2.04	1.609	1.47
MreB	36.311	142.018	87.162	50.251	35.36	29.101	23.719	24.197	13.826	13.553	6.571	8.623	5.404	9.409	5.133	13.285	5.843	6.502	5.521	4.423	3.612	4.744	6.119	2.765	1.309
DnaKHsp70	24.798	83.67	213.878	41.184	28.452	23.699	16.68	17.728	12.206	11.176	4.075	7.849	5.279	9.283	5.776	12.94	6.32	4.816	5.404	3.352	4.423	5.36	5.021	1.427	1.139
FtsA	22.284	47.399	40.859	160.018	97.065	23.719	16.149	18.722	14.636	14.732	4.804	8.68	9.316	7.094	6.32	9.657	5.915	5.279	4.51	3.73	1.833	2.976	4.075	11.596	2.04
PilM	15.936	36.008	29.671	100.783	146.724	17.728	9.21	18.441	12.86	13.72	4.678	10.127	6.119	7.156	4.343	8.422	9.35	7.07	5.221	3.507	4.343	2.551	3.244	27.867	1.386
ParM/StbA	12.717	27.946	24.264	25.233	16.873	133.288	14.592	13.816	10.925	11.107	4.343	9.361	6.32	9.272	5.15	6.97	4.269	4.343	4.51	6.075	4.722	4.791	5.279	0.236	1.386
EutA	9.987	22.62	16.118	17.391	11.251	15.33	389.137	9.327	13.41	16.722	4.269	4.615	2.604	9.21	3.817	6.805	2.303	3.381	4.343	10.232	3.863	2.976	4.51	2.513	2.957
DDR	8.335	21.894	17.322	22.237	17.356	13.228	12.94	583.247	6.502	15.936	3.54	3.612	6.166	9.721	5.319	7.775	4.343	5.051	5.599	2.526	2.04	4.343	4.605	0.821	2.04
BcrAD/BadFG	7.799	12.983	11.884	12.94	15.713	9.485	11.959	5.279	296.34	7.236	4.678	12.429	3.963	8.074	3.016	14.201	3.689	5.339	7.506	5.221	10.871	10.483	3.817	0.511	18.777
ppx_gppa	7.562	13.074	10.925	14.614	14.002	9.485	18.965	14.509	7.339	260.885	2.996	2.04	2.501	6.725	22.62	7.849	4.343	3.912	2.939	4.2	1.05	1.661	2.207	1.347	3.507
DUF1464	6.266	5.843	4.934	4.605	4.135	4.656	3.507	1.897	5.547	3.772	296.34	3.817	5.185	2.207	0.4	7.293	2.781	2.674	8.079	11.418	0.968	1.661	2.303	1.897	1.386
AnmK	6.032	8.079	7.354	8.468	9.641	9.115	5.714	3.324	12.148	2.207	3.863	291.33	3.147	2.749	2.882	11.652	2.919	2.303	5.655	6.812	7.581	4.343	0.315	1.079	4.2
Pan_Kinase	5.684	5.655	6.377	5.952	5.745	5.745	4.605	5.714	5.051	4.135	2.847	2.996	156.863	8.335	4.343	9.657	5.684	7.118	4.017	7.25	1.204	1.897	1.772	0.598	2.12
Glu_Mutase	5.627	9.028	8.948	8.079	6.438	8.517	7.195	10.009	11.564	7.024	1.661	2.718	8.146	313.152	5.714	11.418	5.36	7.775	5.036	6.571	1.833	0.942	15.713	0.821	1.833
gda1/cd39	4.962	4.867	4.841	4.867	3.772	5.15	6.98	5.521	3.058	24.335	1.139	2.83	2.538	5.627	269.913	5.36	6.075	4.135	2.207	4.269	0.545	0.462	0.329	1.609	1.022
FGGY	4.744	13.553	13.978	11.043	9.21	6.075	8.377	5.473	15.936	8.294	6.571	13.174	7.524	9.987	5.167	211.368	8.805	6.571	12.289	6.725	8.079	8.874	4.343	0.274	1.022
Hexokinase	4.636	6.166	6.075	7.024	9.79	4.343	4.2	4.2	4.135	5.449	2.364	2.12	5.279	5.382	5.991	10.724	282.119	19.499	16.281	4.269	0.654	2.847	1.661	0.598	1.05
Glucokinase	4.605	7.002	6.571	5.426	7.024	4.733	4.135	3.863	6.075	5.521	1.609	1.609	7.013	9.641	5.24	8.948	20.318	208.254	30.29	7.929	0.734	1.609	3.963	0.916	0.713
ROK	4.51	5.298	4.2	5.259	5.684	4.135	4.017	5.051	7.621	2.937	8.874	5.497	4.269	4.423	1.833	12.717	17.951	29.995	165.45	11.675	2.631	1.966	2.865	1.05	1.609
Acetate Kinase	4.343	4.51	3.612	4.017	3.101	5.455	10.82	2.04	5.809	5.426	12.405	5.521	5.167	6.166	5.067	6.075	4.934	8.568	11.761	291.042	2.703	3.244	0.261	1.109	1.079
Pep_M22	4.017	3.65	4.2	1.079	3.016	3.912	3.324	1.609	11.533	1.427	1.204	6.377	1.715	1.833	0.58	7.419	1.171	0.58	2.696	3.507	239.522	10.127	0.223	1.204	1.897
Carbamoyl_Trans	3.058	5.878	5.809	4.269	2.9	4.768	3.037	3.73	8.948	1.772	1.427	4.605	2.453	1.427	0.371	8.74	2.354	2.957	1.897	3.442	10.982	334.791	0.562	0.994	2.303
Hydantoinase	2.749	7.143	6.32	4.976	4.343	6.266	4.906	5.298	5.714	3.411	1.238	0.58	2.604	16.986	0.994	6.97	3.037	5.203	4.269	1.273	0.968	1.661	296.34	0.942	1.109
T2SSP	1.309	2.207	1.022	11.251	26.172	0.186	2.207	0.598	0.371	1.347	1.273	1.109	0.274	0.261	0.635	0.288	0.616	1.05	1.139	0.844	1.079	0.545	2.303	158.136	0.821
2H_CoA_red	1.022	1.309	0.511	1.772	1.715	1.171	2.749	1.966	20.03	3.963	1.079	3.194	1.772	1.427	1.109	0.673	0.916	0.462	1.609	1.109	1.833	2.501	0.301	1.204	201.038

Table S4. Strains and Plasmids Used in This Study

Strain	Genotype	Source
yPS003	W303 (ura3 ade2-1 his3-11,15 leu2-3,112 trp1-1 Mata BUD4 GLK1-msfGFP::spHIS5)	*This Study*
yPS031	W303 (ura3 ade2-1 mCherry::HIS leu2-3,112 trp1-1 Mata BUD4)	*This Study*
yPS033	W303 (ura3 ade2-1 Citrine::HIS leu2-3,112 trp1-1 Mata BUD4)	*This Study*
yPS041	W303 (ura3 ade2-1 Citrine::HIS leu2-3,112 trp1-1 Mata BUD4 glk1Δ::HPH)	*This Study*
yPS106	W303 (ura3 ade2-1 his3-11,15 leu2-3,112 trp1-1 Mata BUD4 Glk1(F3S))	*This Study*
yPS108	W303 (ura3 ade2-1 his3-11,15 leu2-3,112 trp1-1 Mata BUD4 GLK1(F3S,K182A))	*This Study*
yPS109	W303 (ura3 ade2-1 his3-11,15 leu2-3,112 trp1-1 Mata BUD4 Glk1(K182A))	*This Study*
yPS110	W303 (ura3 ade2-1 his3-11,15 leu2-3,112 trp1-1 Mata BUD4 Glk1(F3S)-msfGFP::URA)	*This Study*
yPS111	W303 (ura3 ade2-1 his3-11,15 leu2-3,112 trp1-1 Mata BUD4 GLK1(F3S,K182A)-msfGFP::URA)	*This Study*
yPS112	W303 (ura3 ade2-1 his3-11,15 leu2-3,112 trp1-1 Mata BUD4 Glk1(K182A)-msfGFP::URA)	*This Study*
yPS113	W303 (ura3 ade2-1 Citrine::HIS leu2-3,112 trp1-1 Mata BUD4 Glk1(F3S))	*This Study*
yPS116	W303 (ura3 ade2-1 Citrine::HIS leu2-3,112 trp1-1 Mata BUD4 Glk1(K182A))	*This Study*
yPS117	W303 (ura3 ade2-1 Citrine::HIS leu2-3,112 trp1-1 Mata BUD4 Glk1(F3S,K182A))	*This Study*

Plasmid	Description	Source
pSUMO-Glk1	his6-SUMO tagged *S. cerevisiae* Glucokinase in T7 expression vector (AMP)	*This Study*
pSUMO-caglGlk1	his6-SUMO tagged *C. glabrata* Glucokinase in T7 expression vector (AMP)	*This Study*
pSUMO-caalGlk1	his6-SUMO tagged *C. albicans* Glucokinase in T7 expression vector (AMP)	*This Study*
pSUMO-scpoHxk1	his6-SUMO tagged *S. pombe* Glucokinase in T7 expression vector (AMP)	*This Study*
pSUMO-nacaGlk1	his6-SUMO tagged *N. castellii* Glucokinase in T7 expression vector (AMP)	*This Study*
pSUMO-laklGlk1	his6-SUMO tagged *L. kluyveri* Glucokinase in T7 expression vector (AMP)	*This Study*
pSUMO-vapoGlk1a	his6-SUMO tagged *V. polysporus* Glucokinase-1 in T7 expression vector (AMP)	*This Study*
pSUMO-vapoGlk1b	his6-SUMO tagged *V. polysporus* Glucokinase-2 in T7 expression vector (AMP)	*This Study*
pSUMO-kllaGlk1	his6-SUMO tagged *K. lactis* Glucokinase in T7 expression vector (AMP)	*This Study*
pSUMO-ergoGlk1	his6-SUMO tagged *E. gossypii* Glucokinase in T7 expression vector (AMP)	*This Study*
pSUMO-Hxk1	his6-SUMO tagged *S. cerevisiae* Hexokinase-1 in T7 expression vector (AMP)	*This Study*
pSUMO-Hxk2	his6-SUMO tagged *S. cerevisiae* Hexokinase-2 in T7 expression vector (AMP)	*This Study*
pSUMO-scpoHxk2	his6-SUMO tagged *S. pombe* Hexokinase in T7 expression vector (AMP)	*This Study*
pSUMO-yaliGlk1	his6-SUMO tagged *Y. lipolytica* Glucokinase in T7 expression vector (AMP)	*This Study*
pSUMO-dehaGlk1	his6-SUMO tagged *D. hansenii* Glucokinase in T7 expression vector (AMP)	*This Study*
pSUMO-hauvGlk1	his6-SUMO tagged *H. uvarum* Glucokinase in T7 expression vector (AMP)	*This Study*
pSUMO-asruGlk1	his6-SUMO tagged *A. rubescens* Glucokinase in T7 expression vector (AMP)	*This Study*

Movie captions

Movie S1: Glk1-GFP Polymerization is Induced by Glucose. Glk1-GFP cells grown to stationary phase were loaded into a flow cell. At the start of the movie, CSM-glucose medium is flowed over the cells, inducing Glk1 polymerization. The movie is a maximum intensity projection of a confocal z-stack. Images were taken at 5-second intervals. Movie begins 20 seconds before glucose addition, which occurs at 0 seconds.

Movie S2: Glk1-GFP Depolymerizes When Glucose is Removed. Glk1-GFP cells grown to saturation were loaded into a flow cell and washed into glucose-containing medium. At the start of the movie, glucose is washed out by washing the cells into CSM medium with no carbon source. The movie is a single confocal slice with continuous capture. Images were taken at 100 ms intervals. Movie begins 10 seconds before glucose withdrawal, which occurs at 0 seconds.